AIAA JOURNAL
Vol. 41, No. 8, August 2003

Hybrid Simulation Approach for Cavity Flows: Blending, Algorithm, and Boundary Treatment Issues

R. A. Baurle* and C.-J. Tam†
Taitech, Inc., Beavercreek, Ohio 45430
and
J. R. Edwards‡ and H. A. Hassan§
North Carolina State University, Raleigh, North Carolina 27695

The maturation of high-performance computer architectures and computational algorithms has prompted the development of a new generation of models that attempt to combine the robustness and efficiency offered by the Reynolds averaged Navier–Stokes equations with the higher level of modeling offered by the equations developed for large eddy simulation. The application of a new hybrid approach is discussed, where the transition between these equation sets is controlled by a blending function that depends on local turbulent flow properties, as well as the local mesh spacing. The utilization of local turbulence properties provides added control in specifying the regions of the flow intended for each equation set, removing much of the burden from the grid-generation process. Moreover, the model framework allows for the combination of existing closure model equations, avoiding the difficulty of formulating a single set of closure coefficients that perform well in both Reynolds averaged and large eddy simulation modes. Simple modifications to common second-order accurate Reynolds averaged Navier–Stokes algorithms are proposed to enhance the capturing of large eddy motions. Incompressible Poiseuille flow, supersonic base flow, and supersonic flow over recessed cavities were considered to evaluate various aspects of the proposed model and computational framework. Calculations using another hybrid approach (detached eddy simulation) were also performed for comparison.

Nomenclature

a_{ij}	=	matrix of normalized velocity variances and covariances
b	=	law of the wall intercept
$CD_{k\omega}$	=	cross-diffusion term for the specific turbulent dissipation rate
C_d	=	constant for the destruction term of k
C_{DES}	=	constant for the detached eddy simulation (DES) length scale
C_p	=	pressure coefficient
C_s	=	constant for the Smagorinsky viscosity coefficient
C_μ	=	constant for the turbulent viscosity coefficient
C_{ω_p}	=	constant for the production term of ω
c	=	constant for the gradient sensor
D	=	cavity depth
d	=	distance to the nearest solid surface
F	=	blending function
F^c, F^d, F^u	=	central, dissipative, and upwind contributions to the inviscid fluxes
f	=	joint normal distribution function
h	=	channel height
k	=	turbulent kinetic energy
ℓ	=	turbulent length scale
m	=	normalized cavity mass
n, β	=	constants for the latency parameter of Speziale[6]
P	=	pressure
P_k	=	production term for the turbulent kinetic energy
P_ω	=	production term for the specific turbulent dissipation rate
q	=	MUSCL extrapolated variable
R	=	sting base radius
r	=	numerical dissipation reduction factor
r, θ	=	polar coordinates
t	=	time
u_i	=	velocity
u_τ	=	friction velocity
V	=	turbulent velocity scale
v_i	=	velocity normalized with the rms of its fluctuation
x, y, z	=	Cartesian coordinates
Δ	=	subgrid length scale
δ_{ij}	=	Kronecker delta
δ_+, δ_-	=	finite difference operators (forward, backward)
ϵ	=	turbulent dissipation rate or generic small number
η	=	blending function argument
κ	=	MUSCL interpolation constant or law of the wall slope
μ	=	viscosity coefficient
ν	=	specific viscosity coefficient
ρ	=	density
σ_{cd}	=	constant for the turbulent cross-diffusion term of ω
σ_k	=	constant for the turbulent diffusion term of k
σ_ω	=	constant for the turbulent diffusion term of ω
τ	=	residence time
τ_{ij}	=	stress tensor
ψ	=	gradient sensor
ω	=	specific turbulent dissipation rate
∇	=	gradient operator

Presented as Paper 2001-2562 at the AIAA 15th Computational Fluid Dynamics Conference, Anaheim, CA, 11–14 June 2001; received 17 September 2002; revision received 19 April 2003; accepted for publication 19 April 2003.

*Senior Research Scientist, Computational Fluid Dynamics Group. Senior Member AIAA.
†Research Scientist, Computational Fluid Dynamics Group. Member AIAA.
‡Associate Professor, Mechanical and Aerospace Engineering. Senior Member AIAA.
§Professor, Mechanical and Aerospace Engineering. Associate Fellow AIAA.

Subscripts

av	=	averaged quantity
blk	=	bulk quantity for the channel flow
i, j, k, n	=	spatial coordinates or cell indices
t	=	turbulent quantity
η	=	Kolmogorov scale
∞	=	freestream quantity

Superscripts

L, R	=	left or right states of the MUSCL scheme
$'$	=	time-averaged fluctuating component
$''$	=	Favre-averaged fluctuating component
$+$	=	wall unit
$-$	=	time-averaged quantity
$\sim$	=	Favre-averaged quantity

Introduction

TO better predict flows that are fundamentally unsteady at scales comparable to that of the mean flow, a large eddy simulation (LES) solution strategy is often preferred over traditional Reynolds averaged Navier–Stokes (RANS) methodologies. The LES approach for turbulence closure attempts to resolve the large-scale components of turbulence while modeling the smaller scales. There are several factors that suggest that LES is a good compromise between traditional Reynolds averaged solution approaches and direct numerical simulation (DNS). First, most of the transport of mass, momentum, and energy (on the order of 90%) is done by the large eddies, whereas the primary role of the small eddies is to dissipate these fluctuations. Hence, it is the large eddies that tend to interact directly with the mean flow. Second, the small eddies are less dependent on boundary conditions and flow type than are the large-scale eddies. Thus, the modeling developed for small scales should be more generally applicable than models developed for the entire range of turbulent scales. Unfortunately, the computational costs of LES often prohibit its use as an engineering design tool for practical applications. This is particularly true for attached wall-bounded regions at modest to high Reynolds numbers. A comparison of the LES and RANS equations reveals that the overall structure of each equation set is quite similar. Therefore, existing RANS solvers can (in principle) be readily extended to function as LES solvers. This observation has led many to consider the possibility of blending LES and RANS approaches into a single modeling strategy for complex flows of engineering interest.

The present effort is aimed at illustrating the capabilities of hybrid RANS/LES models for simulating the complex flow physics associated with recessed cavity flows. This application is perfectly suited for a hybrid RANS/LES treatment because the flow unsteadiness induced by the cavity is strong and self-sustaining. The flows in and around recessed cavities are remarkably complicated, with internal and external regions that are coupled via self-sustained shear layer oscillations. Computational models applied to these devices must be able to capture coherent shed vortices, unsteady shock waves, and interactions between the external shed vortices and vortices that reside within the cavity. These characteristics depend strongly on the shape and size of the cavity, incoming Mach number, and, to a smaller extent, the Reynolds number. RANS techniques are notorious for their inability to predict unsteady flowfields in and around recessed cavities.[1–3] Traditional RANS models have no mechanism for distinguishing between different scales of turbulent eddy motion. Thus, all unsteady motions tend to be interpreted as turbulence and "damped" out by the additional viscosity coefficient introduced by the model. This phenomenon often limits the information that can be gathered from RANS approaches to steady-state data, which is of little use when analyzing changes in flow characteristics that result from a change in cavity shape. LES, on the other hand, offers a natural distinction between the resolved scales and unresolved scales based on grid resolution. This distinction allows LES to predict flow unsteadiness when traditional RANS approaches do not.

A variety of issues must be addressed when developing hybrid RANS/LES closure models. Some of these issues include methods for blending the RANS and LES model equations, control of excessive numerical dissipation, and the treatment of inflow/outflow boundary conditions (in LES regions). With the exception of Ref. 4, previous hybrid RANS/LES model development has focused almost exclusively on blending details[5–8] with considerably less attention being placed on the remaining issues involved. The present effort addresses each of these factors with equal importance.

Hybrid RANS/LES Formulation

Speziale[6] was an early contributor in the development of hybrid RANS/LES closure models. Speziale formulated a hybrid strategy in which the modeled turbulent stress tensor is evaluated by reducing the Reynolds stress tensor in regions where the grid spacing, Δ, approaches the Kolmogorov length scale ℓ_η, that is,

$$\tau_{ij} = [1 - \exp(-\beta\Delta/\ell_\eta)]^n \tau_{ij}^{\mathrm{RANS}} \tag{1}$$

As the grid spacing approaches the Kolmogorov scale, the turbulent stresses are reduced and the equation set approaches that of a DNS. In regions where the grid spacing is much larger than the Kolmogorov scale, the original RANS stresses are recovered. Any trusted RANS model can be blended with this approach, although Speziale recommended the use of a two-equation RANS model with nonequilibrium effects incorporated via an explicit algebraic stress model. Speziale also warned against the use of test filters because the inversion of filtered quantities can be mathematically ill posed. Examples of applications that employ this blending strategy may be found in Refs. 7 and 9. A variant of this strategy, limited numerical scales (LNS), has been introduced by Batten et al.[8,10] In the LNS formulation, the latency parameter of Eq. (1)

$$[1 - \exp(-\beta\Delta/\ell_\eta)]^n \tag{2}$$

is replaced with

$$\frac{\mathrm{minimum}[(\ell \times V)^{\mathrm{SGS}}, (\ell \times V)^{\mathrm{RANS}}]}{(\ell \times V)^{\mathrm{RANS}}} \tag{3}$$

where $(\ell \times V)^{\mathrm{SGS}}$ is the length-scale/velocity-scale product of some subgrid-scale (SGS) model and $(\ell \times V)^{\mathrm{RANS}}$ is the corresponding product for the given RANS model. The motivation for this change is threefold. First, the length-scale/velocity-scale product is the primary parameter that effects the turbulent viscosity levels. Therefore, this parameter is expected to play a strong role in the blending strategy. Second, because the original function proposed by Speziale[6] compares mesh spacing with the Kolmogorov scale, it reduces the RANS stresses significantly only in regions where the grid resolution approaches that required for DNS. It would seem desirable to design a blending function that senses LES regions more directly. Finally, the latency parameter of Batten et al.[8,10] requires no additional closure coefficients.

A second blending strategy, referred to as detached eddy simulation (DES), has been proposed by Spalart et al.[5] In DES, the RANS equations are invoked near solid surfaces where the flow is attached, whereas the LES equations are invoked for separated (detached) flow regions. The development of this variant was motivated by the immense grid requirements associated with resolving eddy motions in wall-bounded regions of the flow. Moreover, attached wall-bounded flows are often well predicted by traditional RANS models, as compared with free shear flows and separated wall-bounded flows. The original DES formulation was built around the Spalart–Allmaras one-equation turbulence model.[11] The blending of this RANS model with LES is accomplished by altering the length scale that appears in the destruction term of the turbulence transport equation. The base RANS model uses the wall distance d as the turbulence length scale. The DES model replaces this length scale with the minimum of d and some measure of the maximum length associated with the local grid element. This definition of the turbulence length scale ensures

that the RANS equations are employed near solid surfaces when the grid aspect ratio is typically high. The DES approach was later extended to a two-equation (Menter[12] k–ω) formulation by Strelets.[4] The two-equation variant of DES replaces the turbulence length scale appearing in the destruction term of the turbulence kinetic energy equation

$$\ell^{\mathrm{RANS}} = k^{\frac{1}{2}} \big/ C_d \omega = k^{\frac{3}{2}} \big/ C_d \epsilon \tag{4}$$

for the k–ω model and k–ϵ model, respectively, with the DES length scale described earlier, that is,

$$\ell = \mathrm{minimum}\left[\ell^{\mathrm{RANS}}, C_{\mathrm{DES}}\Delta\right] \tag{5}$$

C_d is the constant appearing in the dissipation term of the turbulence kinetic energy (TKE) equation. This constant is typically 1.0 for the k–ϵ model and is either 1.0 or 0.09 for the k–ω model depending on how ω is defined. For structured grids aligned with an x, y, z coordinate system, $\Delta = \mathrm{maximum}\ (\Delta x, \Delta y, \Delta z)$. Examples of applications that have invoked the DES model may be found in Refs. 4 and 13–15.

One potential drawback to the DES approach that was highlighted in the original reference (Ref. 5) involves the situation where the grid is locally refined in all directions in a region not intended to be handled by LES. This often occurs in structured grids where refinement is required in some region of high geometric curvature. When the grid is locally refined in all directions along a solid boundary, the eddy viscosity associated with the approach boundary layer is substantially reduced, with no mechanism to transfer the modeled (unresolved) turbulence energy into resolved turbulence energy. In effect, the flow locally relaminarizes and corrupts the turbulent boundary-layer properties farther downstream. Most DES applications to date have been centered around external flow applications where this situation can usually be avoided. This can represent a severe limitation, however, for complex internal flow applications where "parasitic" local refinements are often unavoidable when structured grids are employed.

Based on this observation, one would prefer to base the blending strategy on local flow properties as well as grid spacing, to take some of the burden away from the grid generation process. The intended use of DES was to have the model act in RANS mode for attached wall-bounded flow regions and blend into an LES formulation for detached (separated or free shear) flow regions. This scenario is quite similar to what Menter[12] faced in his work toward blending the k–ω and k–ϵ models. Menter sought to develop a single RANS turbulence model that retained the robustness and accuracy of the Wilcox k–ω model,[16,17] for wall-bounded viscous regions, while enforcing a k–ϵ model away from solid surfaces to avoid the undesirable dependence of k–ω model results on freestream values of ω. To achieve this goal, Menter[12] linearly combined the k–ω and k–ϵ model equations, that is,

$$\text{Menter model} = (F)[k-\omega \text{ model}] + (1-F)[k-\epsilon \text{ model}] \tag{6}$$

with a blending function designed to yield a value of 1 near solid surfaces and to transition rapidly to 0 in the outer portion of the boundary layer and regions of free shear. Menter devised the following functional form for F to meet these criteria:

$$F = \tanh(\eta^4), \qquad \eta = \mathrm{maximum}\left(\frac{\ell^{\mathrm{RANS}}}{d}, \frac{C_d \ell^{\mathrm{RANS}}}{k^{\frac{1}{2}} d^2} 500\nu\right) \tag{7}$$

The first argument compares the RANS turbulence length scale with the distance to the nearest wall. This ratio is 2.5 in the logarithmic portion of the boundary layer and approaches zero near the boundary-layer edge. The second term is designed to ensure that F does not go to zero in the laminar sublayer. The hybrid RANS/LES model developed in this effort has been built around the same framework. The desired model should invoke a RANS treatment near solid surfaces and an LES treatment in separated and free shear regions. The choice of RANS model can be any one-equation or two-equation model that includes a transport equation for the turbulence kinetic energy. The choice of LES (SGS) model can be any one-equation model that includes a transport equation for the SGS turbulence kinetic energy. The hybrid model is then defined by a linear combination of each model equation set:

$$\begin{aligned}\text{Hybrid RANS/SGS TKE equation} &= (F)[\text{RANS TKE equation}] \\ &\quad + (1-F)[\text{SGS TKE equation}] \\ \text{Hybrid RANS/SGS viscosity} &= (F)[\text{RANS viscosity}] \\ &\quad + (1-F)[\text{SGS viscosity}]\end{aligned} \tag{8}$$

An algebraic SGS model (or even a monotone integrated LES) can also be considered by constructing a production/destruction balance equation for the SGS TKE that recovers the desired algebraic viscosity model. Preliminary results obtained with this hybrid approach were reported in Refs. 18 and 19. One issue that later surfaced with this formulation involves the behavior of the blending function in freestream regions. The blending function given by Eq. (7) always forces an LES treatment away from walls even if the grid is too coarse to support LES, leading to excessive levels of modeled turbulent viscosity in the unperturbed freestream. This problem was overcome by redefining the blending function using ideas borrowed from the LNS hybrid approach:

$$F = \mathrm{maximum}\left[\tanh(\eta^4), F_{\mathrm{LNS}}\right] \tag{9}$$

where

$$F_{\mathrm{LNS}} = \mathrm{AINT}\left[\mathrm{minimum}\left(\frac{\text{SGS viscosity}}{\text{RANS viscosity}}, 1.0\right)\right] \tag{10}$$

In this expression, AINT represents the FORTRAN 90 intrinsic function used to truncate the fractional portion of its argument. Hence, F_{LNS} is zero if the SGS viscosity is less than the RANS viscosity and is one otherwise. The LNS-inspired portion of the blending function ensures that the RANS equations are retained if the SGS viscosity is greater than the RANS viscosity.

In addition to removing some of the burden from the grid-generation process, the proposed approach for building hybrid RANS/LES formulations also avoids the difficulty with developing a single set of closure coefficients that must function effectively in both RANS and LES modes. For instance, the DES formulations to date have frozen all closure coefficients from the parent RANS model except for the coefficient multiplying the dissipation term in the TKE (or Spalart–Allmaras[11] viscosity) equation. As discussed in at least one previous work,[20] this practice may not yield an optimal closure equation when in LES mode. The present model, on the other hand, is intended to combine any trusted (preexisting) RANS turbulence model with any preexisting SGS closure model. In effect, the burden has been shifted from the determination of appropriate closure coefficients to the determination of an appropriate blending function for the given application.

Numerical Formulation

All computational results were obtained using the VULCAN Navier–Stokes code. The numerical algorithms and physical models available in this RANS code are quite representative of the class of solvers typically used for high-speed flow computations. The code solves the Reynolds averaged conservation equations appropriate for calorically or thermally perfect gases with a cell-centered finite volume scheme. The equation set can be integrated in a fully elliptic or space-marched manner. The inviscid fluxes can be evaluated with central differences, Roe's flux difference method, or a low diffusion flux vector split scheme. A variety of one-equation and two-equation turbulence models are available to describe the turbulent velocity field, and assumed probability density function (PDF) options exist for modeling turbulence–chemistry interactions. Recent

additions to the code include arbitrary block to block non-C(0) continuous connectivity and block level parallelization using message passing interface. These recent enhancements greatly improve the code's promise for hybrid RANS/LES functionality. Further details describing the code can be found elsewhere.[21,22]

Several modules were added to the VULCAN flow solver to allow it to function in a low-fidelity LES mode. Low fidelity in this context implies that some concessions relating to overall spatial accuracy, complexity of SGS modeling, and rigor of the filtering process were accepted to maintain the robustness and flexibility of the original solver. Given the abundance of existing upwind-biased (second-order accurate) codes presently in use for engineering applications, an exploration of potential modifications to existing algorithms appears warranted. The additional modules include essentially non-oscillatory (ENO) flux limiters, numerical dissipation control, and random forcing for inflow specification.

Flux Limiting

ENO schemes offer a means of removing the local reduction to first-order spatial accuracy associated with popular total variation diminishing (TVD) schemes, such as those currently implemented in VULCAN. ENO schemes utilize data at additional grid nodes to develop a MUSCL-type interpolation procedure that is uniformly second-order accurate, while avoiding spurious oscillations. The present implementation of ENO technology into VULCAN follows the work of Suresh and Huynh,[23] who extended the minmod, Van Leer, and Superbee TVD-limiting schemes to uniform second-order accuracy. The computational overhead in implementing the second-order ENO schemes is minimal, but these limiters require a larger stencil (seven cells) than standard TVD limiters (five cells). Another class of non-TVD limiters are the "smooth" limiters described in Refs. 24 and 25. These limiters are formulated to maintain second-order accuracy in smooth regions of the flow when oscillations are below a certain level. In contrast, TVD limiters locally reduce the order of accuracy when extrema of any magnitude are encountered, which can result in a global reduction of accuracy order. The smooth limiter used in this work has a truncation error (in smooth regions) similar to that of an unlimited $\kappa = \frac{1}{3}$ MUSCL scheme. The higher-order left and right states are given by

$$q^L_{n+\frac{1}{2}} = q_n + \frac{1}{2}\left[\frac{\delta_+\left(\delta^2_- + 2\epsilon\right) + \delta_-\left(2\delta^2_+ + \epsilon\right)}{2\delta^2_- - \delta_-\delta_+ + 2\delta^2_+ + 3\epsilon}\right]$$

$$q^R_{n-\frac{1}{2}} = q_n - \frac{1}{2}\left[\frac{\delta_-\left(\delta^2_+ + 2\epsilon\right) + \delta_+\left(2\delta^2_- + \epsilon\right)}{2\delta^2_+ - \delta_+\delta_- + 2\delta_-\delta_- + 3\epsilon}\right] \tag{11}$$

where

$$\delta_+ = q_{n+1} - q_n, \qquad \delta_- = q_n - q_{n-1} \tag{12}$$

and ϵ is proportional to the cell length cubed. The level of flux limiting is controlled by the constant of proportionality. (Large values reduce the level of flux limiting.) These limiters utilize a stencil of only five cells, but specification of an additional constant is required.

Numerical Dissipation Reduction

The proposed method of numerical dissipation control is based on the observation that any upwind scheme can be written as a central scheme plus some dissipation term, that is,

$$F^u = F^c + F^d \tag{13}$$

here F^u is the upwind-biased flux, F^c is the flux evaluated based on the average of the left and right states of the MUSCL interpolated variables, and F^d is the dissipative component of F^u. The dissipation associated with standard upwind schemes is typically too large for use with LES without excessive grid densities. Thus, one would prefer to use a dissipation contribution that is considerably lower, for example, $r F^d$, where $0 \le r \le 1$. This approach was taken in Ref. 26 for an LES of fully developed flow in a square duct. In general, the numerical dissipation cannot be globally reduced for flows with strong gradients; thus, a more general scheme with dynamic dissipation control could take the following form:

$$F^u = F^c + [r + \psi(1 - r)]F^d \tag{14}$$

where ψ is some sensor of steep gradients. The current strategy for dynamic control of the numerical dissipation is based on using pressure gradient sensors. The idea is to construct a nondimensional pressure gradient parameter that increases the numerical damping near steep pressure gradients, that is,

$$\psi_n = \frac{|\delta_+ P - \delta_- P|}{(1 - c)(|\delta_+ P| + |\delta_- P|) + (c)(P_{n+1} + 2P_n + P_{n-1})} \tag{15}$$

where $0 \le c \le 1$ and n is any coordinate direction (i, j, or k). This parameter is identical to the pressure switch used to add second-order dissipation in many central-differenced scalar dissipation schemes.[27] Other sensors, such as that proposed in Ref. 28, can also be used. The dissipation reduction is applied at each cell interface (to ensure conservation) using the following expression:

$$\psi_{n+\frac{1}{2}} = \text{maximum}(\psi_n, \psi_{n+1}) \tag{16}$$

The preceding formulation yields the desired dissipation behavior for the LES regions. RANS regions, however, will probably require the full dissipation offered by the upwind scheme. This requirement can be realized by redefining the dissipation reduction factor (r) in Eq. (14) to the following:

$$r^* = (1 - F)r + F \tag{17}$$

where F is the switching function that blends the LES ($F = 0$) and RANS ($F = 1$) regions. $F = 1$ implies that $r^* = 1$, and Eq. (14) reverts back to the default upwind formulation irrespective of ψ. Strelets[4] has suggested an alternative blending option in which a central difference approximation (for LES regions) is combined with an upwind approximation (for RANS regions) for the inviscid flux evaluation.

Random Inflow Specification

The transition from RANS to LES in a hybrid solver is the most difficult flow regime to envision because the turbulent eddies are nonexistent upstream of the transition. In fact, the diffusive flowfield present in the RANS region (large eddy viscosities) is expected to inhibit the formation of large eddies as the solver transitions to LES mode. This observation prompted an examination of the influence of random fluctuations entering regions solved using LES. The present effort attempts to define a sequence of random flow properties that, when time-averaged, recovers all known first- and second-order correlations predicted by an upstream RANS calculation.

The approach taken is based on the specification of a PDF. Given a flowfield at some streamwise station generated by a RANS simulation, the first- and second-order velocity correlations (mean velocity components and Reynolds stresses) are used to define a joint normal distribution function for the random velocity components. If each velocity component is normalized by its rms fluctuation,

$$v_1 \equiv u_1/\sigma_1, \qquad v_2 \equiv u_2/\sigma_2, \qquad v_3 \equiv u_3/\sigma_3 \tag{18}$$

then the joint normal distribution can be written as follows:

$$f(v_1, v_2, v_3) = \frac{1}{(2\pi)^{\frac{3}{2}}|\boldsymbol{A}|^{\frac{1}{2}}} \exp\left[-\frac{1}{2}\sum_{i=1}^{3}\sum_{j=1}^{3} a^{-1}_{ij} v_i v_j\right] \tag{19}$$

where $\boldsymbol{A}$ is a matrix defined by the normalized velocity variances and covariances

$$a_{ij} = \begin{cases} 1, & i = j \\ \overline{v'_i v'_j}, & i \ne j \end{cases} \tag{20}$$

Random samples are extracted from this distribution function using the acceptance/rejection method outlined in Ref. 29. The resulting

statistics from the sampling process preserve the first- and second-order correlations given by the RANS profile, provided that the resolved component of the second-order correlations is much larger than its SGS counterpart. In other words, the RANS-based Reynolds stress components are mapped only to the resolved stress tensor in the LES region. Other common approaches prevalent in the literature require additional LES solutions,[30] prescribed power spectrum,[31] or flow recycling.[32] These approaches require more information than can be extracted from a single RANS simulation of the upstream flow.

Test Configurations and Conditions

Plane Poiseuille Flow

The simulation of fully developed flow in a channel is a common benchmark problem for validating LES algorithms. This configuration is an ideal choice for testing algorithm issues because periodic boundary conditions can be applied in both the streamwise and spanwise directions, forgoing the uncertainties associated with specifying inflow/outflow conditions. The use of periodic conditions can be employed in lieu of specifying conditions at inflow/outflow boundaries provided that one replaces the mean pressure gradient (which physically drives the flow) with an equivalent spatially uniform source term that precisely balances the wall shear stress. Another appealing feature of this test case is the insensitivity to choice of SGS model (for the low Reynolds number considered here), which allows algorithm parameters to be independently assessed using a MILES approach. Data available for comparison include measurements,[33] DNS,[34] and LES[35] data. Simulations were carried out on a domain of length $2 \times \pi h$ in the streamwise direction, and $\pi \times h$ in the spanwise direction, where h is the channel height. The dimensions of this domain were chosen to match those used for the DNS reported by Kim et al.[34] The Mach number based on bulk velocity was set to 0.5, and the Reynolds number based on bulk velocity and channel height was 5600. These conditions matched those of Okong'o and Knight.[35] The Mach number was set to an artificially high value due to the compressible solver used in this effort. The resulting static density variation across the channel, however, was less than 4%. Hence, comparisons with the incompressible results of Kim et al.[34] are still meaningful.

The channel walls were treated as isothermal ($T_w = 300$ K), no-slip walls. The grid generated for this simulation consists of $64 \times 96 \times 64$ cells in the streamwise, spanwise, and wall-normal directions, respectively. The grid spacing in terms of wall units are as follows: $\Delta x^+ \approx 32$, $\Delta y^+ \approx 11$, minimum $\Delta z^+ \approx 1$, and maximum $\Delta z^+ \approx 11$. A coarsened version of this grid ($32 \times 48 \times 64$) was used for quick assessments of solution sensitivity to a wide variety of numerical parameters.

The channel flow configuration was primarily used to determine the modifications required to make the second-order accurate (spatial and temporal) algorithms in VULCAN function as an effective LES solver. The lessons learned from this exercise were later applied to the supersonic base flow simulations. All parametric evaluations were performed on the coarse ($32 \times 48 \times 64$) grid. The channel flow LES was initialized by first obtaining a two-dimensional fully developed laminar flow solution. This solution was then expanded in the spanwise (homogeneous) direction and random perturbations were added to the velocity field (maximum perturbation of 20% times the bulk velocity). This forcing procedure is similar to the method used in Ref. 35. The results, using a three-step Runge–Kutta method for time integration and either a Roe scheme or low-diffusion flux vector split scheme (LDFSS) for inviscid flux evaluation, did not show a transition from laminar to turbulent flow. Flux limiter variations, time-step reductions, and higher random forcing levels did little to improve the situation. Instead, a reduction of the numerical dissipation was required to transition the flow. Based on this finding, no explicit SGS model was employed. The flow gradients were benign enough to allow a global reduction of the numerical dissipation, that is, $\psi = 0$ in Eq. (14). The coarse grid allowed values of r as low as 0.1. This value could be reduced further to approximately 0.05 in the fine grid simulations.

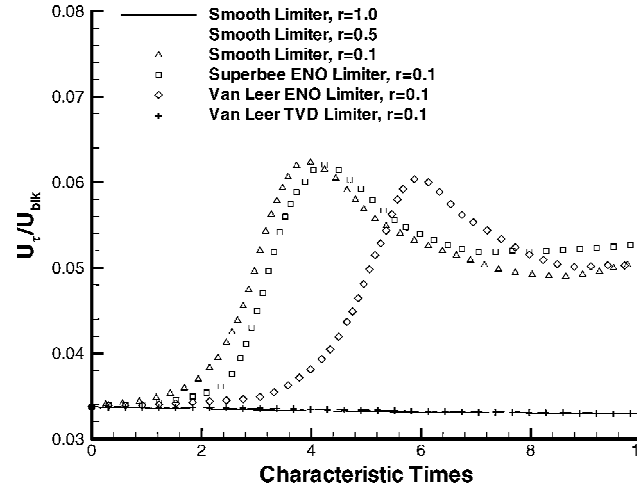

Fig. 1 Sensitivity of friction velocity to LES algorithm coefficients.

The transition from laminar to turbulent flow was monitored by tracking the time history of the friction velocity. The spatial-averaged time history of friction velocity that resulted from parametric variations of several algorithm-dependent parameters is shown in Fig. 1. The transition from laminar to turbulent flow (if it occurs) typically initiates after roughly two to four characteristic eddy-turnover times ($0.5h/u_\tau$). All cases shown in Fig. 1 employed a time-step of 10 μs, Runge–Kutta time integration (three stage), and the flux difference split scheme of Roe (MUSCL interpolation parameter set to $\frac{1}{3}$). Time-step variations, number of Runge–Kutta stages, and choice of upwind scheme (Roe or LDFSS) were not found to be critical parameters. Instead, the critical parameters were values specified for r and the flux limiting method. The baseline case employed the smooth flux limiter with the default numerical dissipation ($r = 1.0$). This choice did not transition the flow to turbulence. Reducing the default numerical dissipation by a factor of two showed that the generation of turbulence was still inhibited, as evidenced by the low levels of friction velocity. A reduction of the default dissipation term by a factor of 10 was required to unlock adequate levels of resolved turbulent energy. A larger reduction in the damping term ($r = 0.05$) was attempted, but a stable solution could not be achieved. The minimum level of dissipation required for numerical stability consistently reproduced the expected levels of friction velocity for this model problem. A similar finding was reported in Ref. 26. This result shows that the upwind-biased numerical dissipation produces an excessive implicit SGS effect and that explicit SGS models would probably degrade the solution further. With the minimum level of artificial dissipation required for stable solutions established, further parametric variations focused on the choice of flux limiter. A common TVD limiter (Van Leer), ENO version of the Van Leer limiter, and the least dissipative of the ENO limiters considered (Superbee-ENO) were tested with r set to 0.1. As shown in Fig. 1, the TVD limiter proved too dissipative to allow turbulent eddies to form from the randomly excited velocity field (at least for the grids considered in this effort). The ENO limiters yielded final friction velocity levels that were comparable with those obtained with the smooth limiter. The results from this study suggest that it is tractable to use a second-order accurate upwind-biased algorithm for LES, provided one controls the dissipation of the scheme and is careful about the choice of flux limiter.

Statistical information was gathered from solutions using both the coarse and fine grids. These simulations were obtained using Roe's method with the smooth limiter, three-stage Runge–Kutta time integration, and the minimum value of r that provided stable solutions (0.1 and 0.05 for the coarse and fine grids, respectively). Statistics were gathered after 20 characteristic times had passed. The data were spatially averaged in the homogeneous directions and temporally averaged over a time span of 20 characteristic eddy-turnover times. Data were averaged in the spatially homogeneous directions before outputting to disk at each sampling interval. The

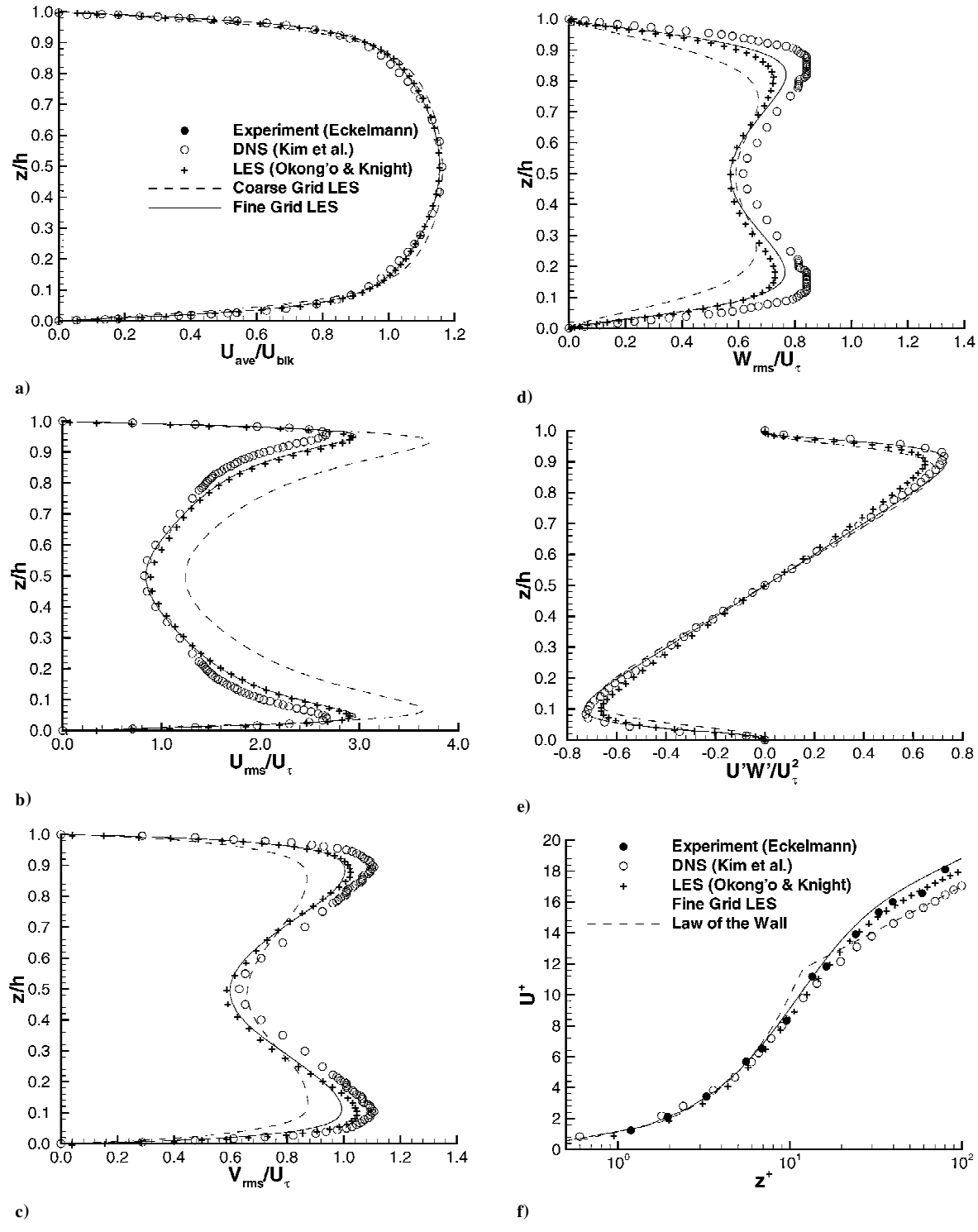

Fig. 2 Channel flow velocity correlations: a) mean streamwise component, b) streamwise fluctuating rms component, c) spanwise fluctuating rms component, d) wall normal fluctuating rms component, e) resolved Reynolds shear stress, and f) mean streamwise component expressed in wall units.

sampling interval was 0.25 ms. This time interval is large relative to the time-step increment (0.01 ms), but small relative to the eddy-turnover time ($\approx$ 50 ms).

Statistical results using both grid densities were compared with the LES results of Okong'o and Knight[35] and the DNS results of Kim et al.[34] The fine grid utilized the same grid distribution reported in the LES results of Okong'o and Knight.[35] Figure 2 shows the statistical data extracted from each data set. The nondimensional mean streamwise velocity is reasonably well predicted on both grid densities. Grid refinement, however, greatly improved the rms predictions. The coarse grid data show somewhat larger turbulence intensities in the streamwise direction, but smaller values for the spanwise and wall normal components. Note that only the fluctuations of the resolved scales are considered in the statistics of the fluctuating components shown here. Thus, one might expect smaller fluctuating rms values for all velocity components on the coarse grid, as compared with the fine grid LES and DNS results. Previous results,[36,37] however, have also shown an overpredictionof the streamwise rms velocity fluctuation when the streamwise resolution is inadequate. Overall, a comparison of the fine grid rms fluctuating velocity with the LES results of Okong'o and Knight[35] suggests that the numerical damping of the second-order accurate

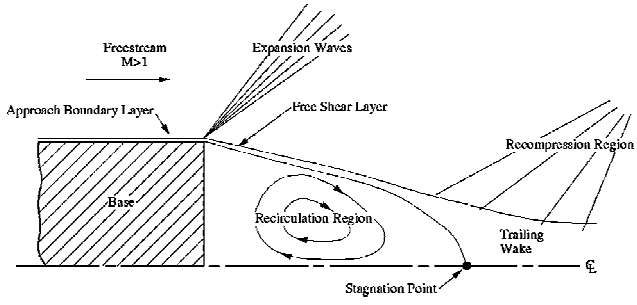

Fig. 3 Schematic of flow structure downstream of sting.

scheme (with reduced dissipation) is comparable to the third-order scheme used in their effort. This finding is significant because it suggests a simple means of controlling the dissipation for real-world applications, where it is difficult to maintain true higher-order accuracy for complex geometries. The average Reynolds number based on the friction velocity of the fine grid LES was 330, which is quite close to the LES result from Okong'o and Knight (333), but somewhat less than the 360 value extracted from the DNS results of Kim et al.[34] The velocity profile (in law of the wall coordinates) is compared with the experimental data of Eckelmann[33] in Fig. 2. Also shown are the velocity profiles extracted from the DNS and unstructured LES data. The LES data from this effort compare well with the experimental data and unstructured LES data. The DNS data, however, more closely resemble the law of the wall using standard wall law constants $\kappa = 0.41$ and $b = 5.5$.

Supersonic Base Flow

The second test case considered was supersonic flow past a blunt annular sting. This application more accurately represents the class of flows envisioned for hybrid RANS/LES methodologies. Extensive measurements have been gathered for this configuration by Herrin and Dutton.[38] Several computational efforts also exist in the literature for this configuration that include the use of pure LES[39] and DES[15] approaches. The accurate prediction of flow separation downstream of blunt bodies is highly relevant to the problem of reducing base drag for missiles and other aerodynamic bodies of revolution. A schematic of the significant flow features associated with supersonic base flow is given in Fig. 3. The supersonic flow expands around the blunt base and eventually reattaches at the axis of symmetry at some station downstream. The rate of expansion is coupled to the turbulence exchange processes between the recirculating flow behind the base and the core flow. The resulting size and shape of the recirculation region behind the base determines the level of base drag. The reattachment of the shear layer on the axis of symmetry forms a recompression shock, which closes out the recirculation region and realigns the flow parallel to the axis of symmetry. Modeling this highly compressible turbulent flowfield has proven to be a difficult test for any turbulence model.[15,39–43] Moreover, many of the essential ingredients for assessing hybrid RANS/LES models are present in this relatively simple flow geometry including transition from attached boundary layer to free shear layer (allows testing of transition functions to control conversion between RANS and LES), relatively strong shocks and expansions (allows testing of concepts for dynamic control of numerical dissipation), and presence of a large region of secondary flow. The one ingredient missing is reattachment of a free shear layer to a solid surface (transition from LES to RANS), which is considered in the recessed cavity flows discussed later.

The experimental setup for the supersonic base flow configuration consists of an annular facility nozzle with a sting mounted along the nozzle axis of symmetry. The sting was mounted such that its base extended just downstream of the facility nozzle exit plane. The facility nozzle dumps into a test section of noncircular cross section, and so an exact reproduction of the experimental test facility would not be practical. Great care was taken during the experiments to ensure a pressure-matched condition was achieved at the nozzle dump plane, thus, minimizing the deflection of the nozzle external surface shear layer. The present simulations took advantage of this fact, and no attempt was made to model the outer surface of the facility nozzle. The computational domain extended $0.5R$ and $10R$ upstream and downstream of the sting base. (The sting base radius $R = 3.175$ cm.) The domain extended $4.144R$ in the radial direction. This domain size was sufficient to ensure that spurious wave reflections from computational boundaries did not interact with the flow region of interest. The freestream Mach number and unit Reynolds number were 2.45 and 5.29×10^7/m. The grid generated for this geometry is given in Fig. 4. The grid zone upstream of the base plane consists of $24 \times 76 \times 120$ cells in the streamwise, radial, and azimuthal directions, respectively. The grid zone downstream of the base plane consists of $132 \times 120 \times 120$ cells. The resolution offered by this grid is slightly more refined than that employed in previous LES works for this geometry.[15,39] The outflow and external boundaries of the domain were specified by a zero-gradient condition. The sting surfaces were treated as no-slip, adiabatic surfaces. The inflow condition was specified using the solution from an a priori RANS simulation (with the Menter[12] k–ω turbulence model) of the flowfield upstream of the sting base. This solution was obtained by marching along the sting, assuming a constant freestream entrance condition, until the boundary-layer displacement and momentum thickness matched (as closely as possible) the measured values of 9.6 and 2.6 cm taken just upstream of the sting base. The resulting velocity profile comparison with the measurements is given in Fig. 5. The comparison between measurement and calculation shows some discrepancies. Grid refinement and turbulence model variations did not show substantial improvements. A similar level of disagreement was also noted by Forsythe and Hoffmann[15] in their attempts

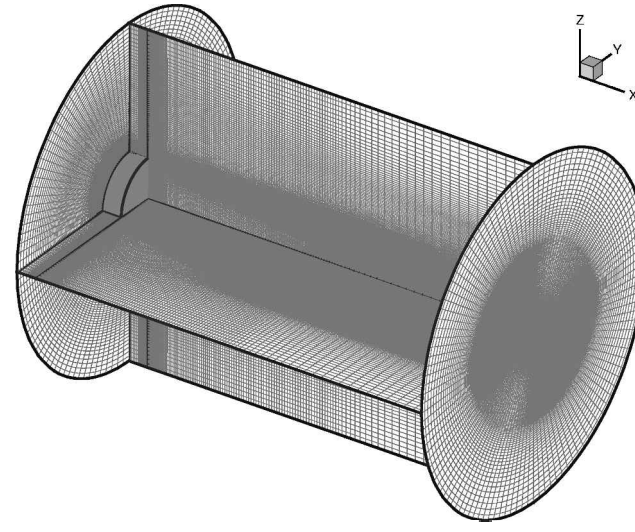

Fig. 4 Grid generated for annular base flow simulations.

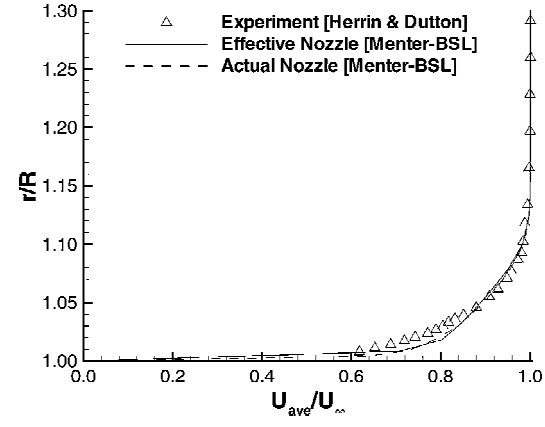

Fig. 5 Boundary-layer velocity profile 1 cm upstream of sting separation.

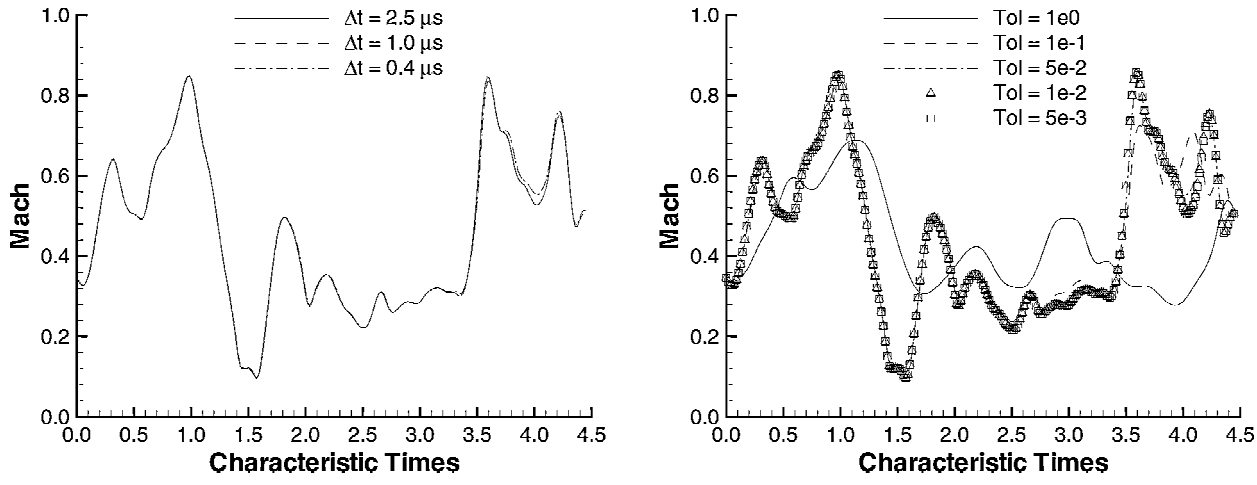

Fig. 6 Mach number time history at axis of symmetry: a) time-step variations and b) convergence tolerance variations.

to match these boundary-layer conditions. One explanation that has been offered to explain this discrepancy is that the measured boundary layer develops under a favorable pressure gradient through the facility nozzle, rather than the zero pressure gradient environment considered here. This hypothesis was tested by performing a RANS simulation of the converging/diverging facility nozzle. The resulting nozzle exit profile exhibited a similar discrepancy, as shown in Fig. 5. At this point, the cause of the discrepancy is not known.

The base flow configuration was used to assess the influence of random inflow forcing that preserves RANS-predicted correlations and to test the dynamic numerical dissipation model. These modules were not relevant for the channel flow problem, although it should be noted that the dynamic dissipation model was applied to the channel flow configuration and found to have no noticeable impact on the results. A detailed comparison of several SGS models with a MILES approach was previously performed by Fureby et al.[39] for this geometry. Their results showed no appreciable differences on first- and second-order statistical moments with variations in SGS model. Based on the results from this reference and the conclusions drawn from the channel flow simulations performed in this effort, no explicit SGS model was employed. The smooth limiter was used for all calculations based on its performance in the channel flow simulations. A coarsened version (coarsened once in each cross-stream coordinate direction) of the grid given in Fig. 4 was used for the parametric evaluations discussed later.

A three-stage Runge–Kutta scheme was initially chosen for time integration, but the time-step constraints required for numerical stability proved too restrictive. Small time steps were required for stability because of the collapsed faces (small volumes) in the mesh along the axis of symmetry. A polar grid topology provided the ideal grid distribution for the present configuration, so that a different time integration strategy was pursued in lieu of switching to a skewed H-topology grid. A separate effort recently added a dual time-stepping scheme to the VULCAN solver. This scheme invokes a diagonalized approximate factorization (DAF) method to integrate in pseudotime, with a three-point backwards finite difference approximation for integration in real time. This scheme provides the desired second-order time-accuracy without a time-step restriction based on numerical stability. The relevant parameters that control the dual time-stepping method are the desired physical time step, subiteration time step, subiteration convergence criteria, and maximum number of subiteration steps. Details on this time integration methodology may be found in Ref. 44.

Several calculations were performed on the base flow configuration to determine the optimal dual time-step parameters that minimized overall turn-around time with sufficient time accuracy. The results of this study are shown in Fig. 6 in the form of time history plots of Mach number along the axis of symmetry at a distance of $1.1875R$ downstream of the sting (other locations showed similar trends). Figure 6a shows that for a fixed relative subiteration convergence tolerance of 0.05, time steps varying from 0.4 to 2.5 μs produce essentially identical solutions. This indicates that the range of time steps tested is sufficiently small to capture the resolved flow physics. Having established the appropriateness of the physical time step, several additional calculations were performed to determine the minimum level of subiteration convergence required to maintain the time accuracy of the solution. These results are shown in Fig. 6b. This study revealed that roughly two orders of magnitude drop in the subiteration residual norm was required to maintain the desired level of time accuracy. A time step of 1 μs with a subiteration convergence tolerance of 0.05 was chosen based on a balance between computational efficiency and desired accuracy.

The channel flow simulations showed that the numerical dissipation associated with the upwind-biased algorithm had to be reduced to resolve the large-scale turbulent structures, at least for the grids used in this study. Moreover, artificial forcing was required to transition the flow from the laminar initial condition to a turbulent flow. The region of interest in the supersonic base flow geometry is the free shear regime downstream of the sting. In the absence of a dissipative RANS eddy viscosity model, the flowfield naturally transitioned from a steady-state turbulent attached flow to an unsteady turbulent flow after separation from the sting base. Artificial forcing was not required to force the unsteadiness, although the effect of artificially exciting the boundary layer was examined. Baseline simulations were performed using the MILES approach with the default level of dissipation. The large turbulent structures in the recirculation region behind the sting and in the developing wake farther downstream were captured without any reduction of the numerical dissipation terms. The effects of adding random inflow conditions and invoking the dynamic dissipation model were examined independently. RANS simulations were also performed for this geometry for comparison with the MILES predictions. The RANS simulations employed the baseline Menter[12] (Menter–BSL) turbulence model with the compressibility correction of Wilcox.[16] The steady-state RANS calculations were performed on a single "pie-slice" of the three-dimensional grid generated for the LESs. All comparisons between LES and RANS calculations were done with consistent values of relevant algorithm parameters. A grid-dependence study using both the fine and coarsened versions of the pie-slice grid showed negligible differences in the final solution. The predicted coarse grid reattachment point and peak Mach number in the recirculation region agreed to within 2% (relative error) of the fine grid result.

The time-averaged Mach contours from the baseline MILES solution are compared with measurements in Fig. 7. The RANS solution is compared with measurements in Fig. 8. The time-averaged data from the MILES solutions represent a combined temporal/spatial average, where the spatial averaging was performed in the homogeneous azimuthal direction. The spatial average was made

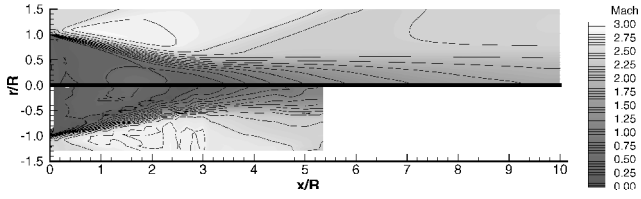

Fig. 7 Mach number contours downstream of sting base: top, LES and bottom, experiment.

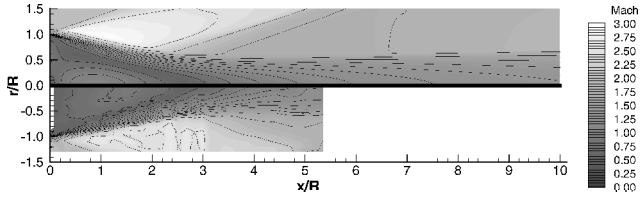

Fig. 8 Mach number contours downstream of sting base: top, RANS and bottom, experiment.

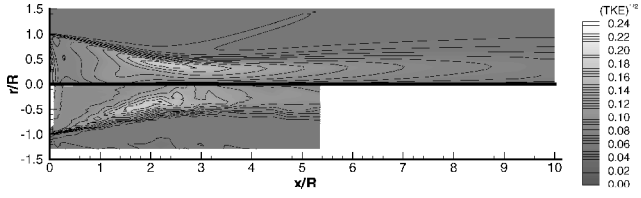

Fig. 9 Turbulence kinetic energy rms contours downstream of sting base: top, LES and bottom, experiment.

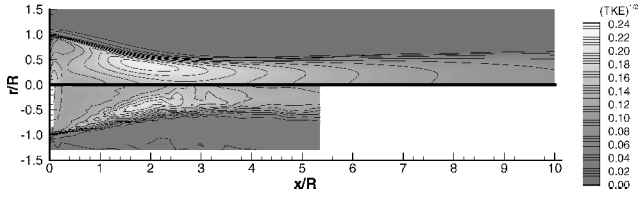

Fig. 10 Turbulence kinetic energy rms contours downstream of sting base: top, RANS and bottom, experiment.

possible by transforming the data to a cylindrical coordinate system $(x, y, z \rightarrow x, r, \theta)$. The spatial average was performed on the transformed variables before writing to disc at at each sampling interval. The data were sampled at 10-μs intervals. The pressure and Mach number were averaged using a standard ensemble (time) average. The remaining flow variables were averaged using a Favre (density-weighted) average for consistency with the RANS data. The experimental data were averaged using standard time averages, but comparisons of standard time and Favre averages using the LES data showed negligible differences. The time-averaged Mach number extracted from the MILES solution compares quite well with the measurements. The overall shape of the recirculation zone and reattachment location are both accurately predicted. The RANS simulation comparison is considerably better than the results reported in Ref. 15 using the Spalart one-equation model[11] and marginally better than the Wilcox k–ω model[17] results from the same reference. The RANS simulation predicts a more rapid expansion downstream of the sting, and as a result, the onset of recompression occurs closer to the sting than the measurements indicate. The Mach number distribution within the recirculation zone is poorly predicted by the RANS model, which shows larger Mach variations and higher reversed flow velocity magnitudes near the centerline. The relatively large Mach gradients within the recirculation zone are the cause of substantial variations in base pressure, as will be shown later.

Comparisons of the measured TKE rms with predictions from the MILES and RANS simulations are shown in Figs. 9 and 10. The

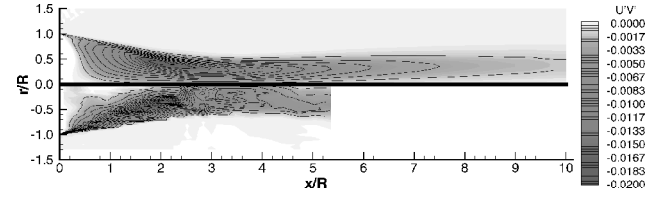

Fig. 11 Reynolds stress contours downstream of sting base: top, LES and bottom, experiment.

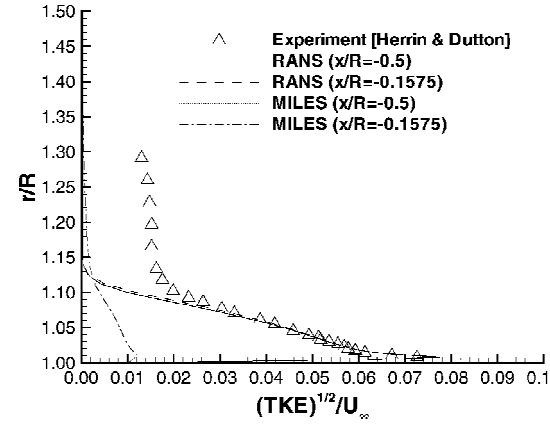

Fig. 12 Time-averaged resolved TKE rms upstream of separation.

LES results only account for the resolved TKE, so that some caution should be exercised when comparing the precise magnitudes of the results, that is, the SGS contribution may not be negligible in some regions of the flowfield. Nevertheless, the resolved TKE results show remarkable agreement with the measurements. The overall TKE magnitude and distribution are well predicted, except near the separation point from the sting. The MILES simulation underpredicts the TKE levels in this thin shear region. An ideal simulation of this flow would have included an LES treatment of the upstream boundary layer to provide initial eddy structures (turbulence energy) at the onset of separation. The present results (and most hybrid RANS/LES concepts) do not take these structures into consideration. Thus, a delay in the production of resolved TKE should be expected. The RANS results do not exhibit this deficiency, but the TKE levels are overpredicted in the recirculation and recompression regions. Finally, the resolved Reynolds shear stress from the MILES results are compared with measured values in Fig. 11. The turbulent shear stress plays a dominant role in determining the mean flow properties; thus, an accurate prediction of this quantity is essential. As was the case with the TKE comparisons, the LES results accurately reproduce the measured values, except in the vicinity of boundary-layer separation from the sting, where the predicted values are too low. Turbulence structures are relatively small in this thin shear region and so one must count on the SGS contribution to play a more prominent role in the region just downstream of separation. (The present grid is much too coarse to resolve the upstream wall-bounded turbulence.)

The effect of random fluctuations is now considered to examine, in a loose manner, the importance of accounting for turbulence structures upstream of the "detached" flow regions. All second-order velocity correlations, that is, the Reynolds stresses, were extracted from a RANS solution at an axial station of $0.5R$ upstream of the sting base. These values, along with the mean flow properties, were used to construct a joint-normal probability density function. Random velocity values were then sampled from this distribution and applied at the inflow plane of the LES domain. Figure 12 shows the resolved TKE obtained by ensemble averaging the flow properties at the inflow plane ($x/R = -0.5$) and a station shortly downstream. The random fluctuations at inflow recovered the values prescribed from the RANS region, but the turbulence levels diminished rapidly at stations farther downstream. A systematic increase in

streamwise and wall-normal resolution showed little improvement. Note that no attempt was made to match the resolved turbulence dissipation term

$$\epsilon = \nu \overline{\frac{\partial u_i'}{\partial x_j} \frac{\partial u_i'}{\partial x_j}} \tag{21}$$

with the value modeled in the upstream RANS region. The stochastic treatment of the random inflow boundary ignores any coherency that is associated with true turbulence eddies. Hence, the resolved turbulence dissipation is expected to be quite large. The rapid depletion of random fluctuations upstream of separation resulted in a negligible difference in turbulence generation after separation from the sting.

The channel flow results discussed earlier required a substantial reduction in the numerical dissipation terms to resolve the turbulence structures of this flow. This was not required in the base flow configuration, but one would expect a benefit from removing excess numerical dissipation in any simulation designed to resolve scales of turbulence. The possibility of shocks with supersonic flows will not, in general, allow a global reduction in the numerical dissipation, as was done for the low-speed channel flow. Instead, the dynamic model that maintains the default level of dissipation near shocks must be employed. Values used for the two model constants were $r = 0.1$ and $c = 0.01$. A sample snapshot of the resulting dissipation weighting factor is given in Fig. 13. Figure 13 clearly shows that the damping control function adds dissipation only in regions of high gradients. Figures 14–16 show a comparison of the predicted mean streamwise velocity, radial velocity, and turbulence kinetic energy profiles (with and without the dissipation reduction model) with measurements. As was indicated in the favorable comparison of Mach number with measurements, the predicted streamwise velocity results (Fig. 14) show the MILES simulations accurately reproduced the overall shape and size of the separation zone downstream of the base, but the velocity magnitude in the reversed-flow region is slightly underpredicted. The predicted radial velocity distributions (Fig. 15) also show a somewhat smaller velocity magnitude within the recirculation zone. As discussed earlier, the generation of turbulence in the shear layer just downstream of separation is delayed due to the absence of resolved TKE within the boundary layer (Figs. 9 and 16). The TKE, however, eventually builds up to a level consistent with the measurements farther downstream. In general, the simulation with reduced numerical dissipation yielded lower resolved turbulence levels than the baseline simulation. This result is not consistent with what was observed in the channel flow simulations. A comparison of flow properties as a function of time showed that oscillations were of higher frequency but smaller amplitude when the numerical dissipation was reduced.

The primary base flow parameter of engineering interest is the pressure distribution (drag) along the base. A comparison of the measured pressure coefficient along the sting base with RANS (Menter–BSL[12]), MILES (default dissipation), and MILES with reduced dissipation are shown in Fig. 17. The pressure coefficient was evaluated based on a reference dynamic and static pressure of 140.059 and 33.225 kPa, respectively. In general, the RANS predictions show a much wider variation of pressure along the base than the measurements and MILES predictions. This is typical of RANS solutions that result in steady-state flows. A steady-state solution

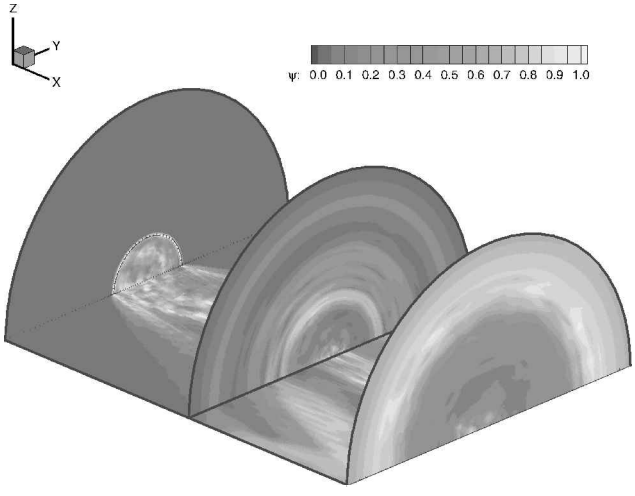

Fig. 13 Snapshot of dynamic dissipation control parameter.

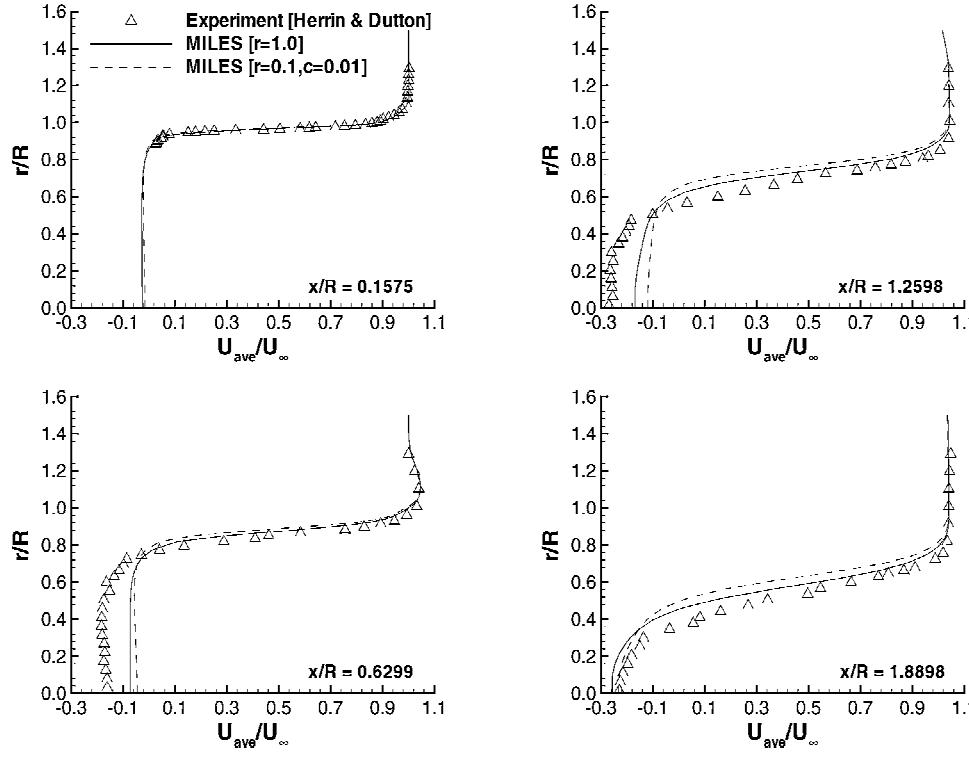

Fig. 14 Comparison of mean streamwise velocity profiles downstream of sting separation, upstream of shear layer reattachment.

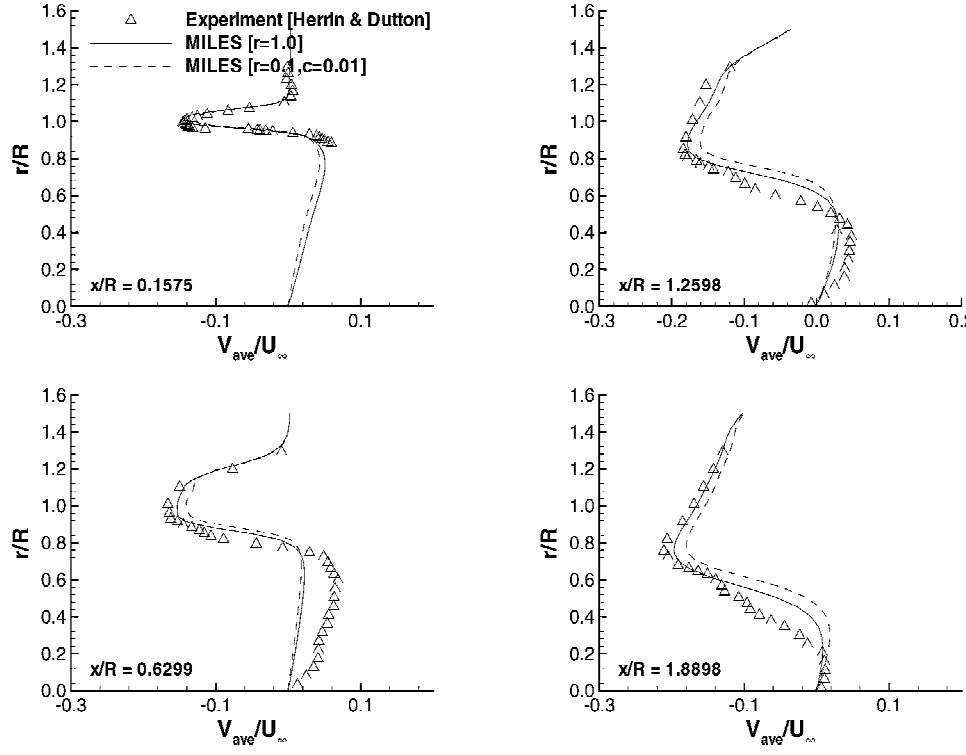

Fig. 15 Comparison of mean radial velocity profiles downstream of sting separation, upstream of shear layer reattachment.

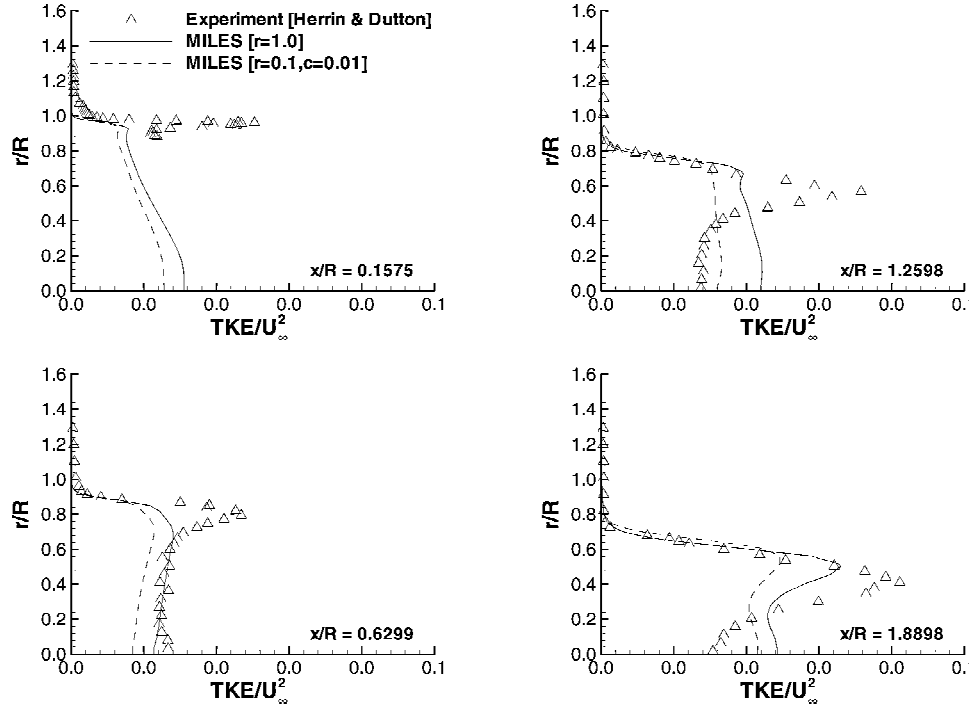

Fig. 16 Comparison of TKE profiles downstream of sting separation, upstream of shear layer reattachment.

of the recirculation zone behind the base yields a fixed (in time) flow pattern within the recirculation zone. In the present case, the recirculating flow tends to stagnate on the sting base at the axis of symmetry (highest pressure) and then accelerate toward the sting lip, resulting in lower pressures as the lip is approached. Near the sting lip, the flow must again turn to align itself with the developing shear layer, resulting in slightly higher pressures near the sting edge. The points of stagnation vary in an unsteady solution, providing a relieving effect that results in considerably smaller variations in time-averaged base pressure. Both MILES predictions show a much improved base pressure distribution when compared with the measurements.

Hybrid RANS/LES Results

The preceding test cases were chosen to provide guidance as to how typical high-speed flow numerics might be modified to function as a low-fidelity LES algorithm. The discussion that follows will focus on the blending between LES and RANS regions using recessed cavity flows as the model problem. Two cavity geometries

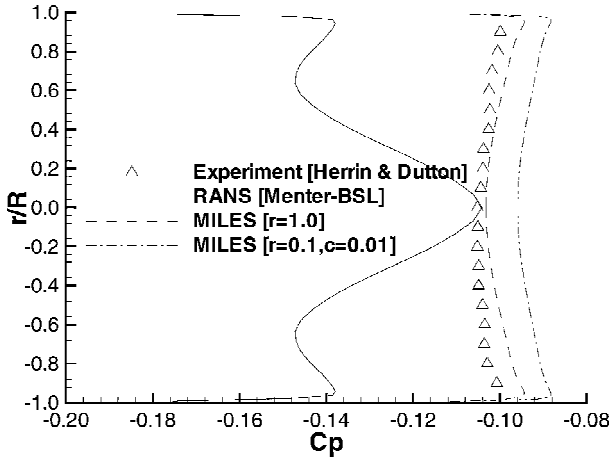

Fig. 17 Comparison of time-averaged pressure coefficient along the sting base.

were considered in this effort. The first cavity configuration was taken from Ref. 45. This case consists of a Mach 2.92 flow over a recessed cavity with a ramped (20-deg) aft surface. This geometry represents a stringent test of the transition from RANS to LES because the cavity feedback mechanism is weak due to the angled aft cavity surface. Shear layer velocity profiles, cavity surface pressure distributions, and profiles (velocity and pressure) in the boundary-layer recovery region are compared with data from measurements. The second case considered was a Mach 2.0 flow over a rectangular ($L/D = 7.76$) cavity considered at the U.S. Air Force Research Laboratory/PRA (AFRL/PRA). The cavity oscillation cycle is quite intense for this configuration, leading to a very complex interaction of flow structures that were captured by the hybrid RANS/LES approach.

In this effort, two parent k–ω models were considered for the RANS portion of the hybrid model. The models chosen were the Menter–BSL[12] and Wilcox[17] models. Expressions for the TKE and eddy viscosity for both models can be written as follows:

$$\frac{\partial}{\partial t}(\bar{\rho}\tilde{k}) + \frac{\partial}{\partial x_j}(\bar{\rho}\tilde{k}\tilde{u}_j) = \frac{\partial}{\partial x_j}\left[\left(\mu + \frac{\mu_t}{\sigma_{k_1}}\right)\frac{\partial \tilde{k}}{\partial x_j}\right] + P_k - C_{d_1}\bar{\rho}\tilde{k}\tilde{\omega}$$

$$\mu_t = C_{\mu_1}\bar{\rho}\frac{\tilde{k}}{\tilde{\omega}} \tag{22}$$

where the production term, P_k, is given by

$$P_k = \mu_t\left[\frac{\partial \tilde{u}_i}{\partial x_j} + \frac{\partial \tilde{u}_j}{\partial x_i} - \frac{2}{3}\delta_{ij}\left(\bar{\rho}\tilde{k} + \mu_t\frac{\partial \tilde{u}_k}{\partial x_k}\right)\right]\frac{\partial \tilde{u}_i}{\partial x_j}$$

$$\approx \mu_t\left(\frac{\partial \tilde{u}_i}{\partial x_j} + \frac{\partial \tilde{u}_j}{\partial x_i}\right)\frac{\partial \tilde{u}_i}{\partial x_j} \tag{23}$$

The approximation made to the production term allows the final hybrid model to reduce precisely to a Smagorinsky model in LES regions when production balances dissipation. The exact production term can be retained if desired. The SGS model chosen was the one-equation model of Yoshizawa and Horiuti[46]:

$$\frac{\partial}{\partial t}(\bar{\rho}\tilde{k}) + \frac{\partial}{\partial x_j}(\bar{\rho}\tilde{k}\tilde{u}_j) = \frac{\partial}{\partial x_j}\left[\left(\mu + \frac{\mu_t}{\sigma_{k_2}}\right)\frac{\partial \tilde{k}}{\partial x_j}\right] + P_k - C_{d_2}\bar{\rho}\frac{\tilde{k}^{\frac{3}{2}}}{\Delta}$$

$$\mu_t = C_{\mu_2}\bar{\rho}\tilde{k}^{\frac{1}{2}}\Delta \tag{24}$$

Multiplying the RANS eddy viscosity and TKE equation by F and the SGS viscosity and TKE equation by $(1 - F)$ yields the desired hybrid model equations:

$$\frac{\partial}{\partial t}(\bar{\rho}\tilde{k}) + \frac{\partial}{\partial x_j}(\bar{\rho}\tilde{k}\tilde{u}_j) = \frac{\partial}{\partial x_j}\left[\left(\mu + \frac{\mu_t}{\sigma_k}\right)\frac{\partial \tilde{k}}{\partial x_j}\right]$$
$$+ P_k - \bar{\rho}\left[(F)C_{d_1}\tilde{k}\tilde{\omega} + (1 - F)C_{d_2}\frac{\tilde{k}^{\frac{3}{2}}}{\Delta}\right]$$

$$\frac{\partial}{\partial t}(\bar{\rho}\tilde{\omega}) + \frac{\partial}{\partial x_j}(\bar{\rho}\tilde{\omega}\tilde{u}_j) = \frac{\partial}{\partial x_j}\left[\left(\mu + \frac{C_{\mu_1}\bar{\rho}(\tilde{k}/\tilde{\omega})}{\sigma_\omega}\right)\frac{\partial \tilde{\omega}}{\partial x_j}\right]$$
$$+ CD_{k\omega} + P_\omega - C_{\omega_d}\bar{\rho}\tilde{\omega}^2$$

$$\mu_t = \bar{\rho}\left[(F)C_{\mu_1}\frac{\tilde{k}}{\tilde{\omega}} + (1 - F)C_{\mu_2}\tilde{k}^{\frac{1}{2}}\Delta\right] \tag{25}$$

where

$$\frac{1}{\sigma_k} = \frac{(F)}{\sigma_{k_1}} + \frac{(1 - F)}{\sigma_{k_2}}$$

$$CD_{k\omega} = \begin{cases} 0; & \text{Wilcox}^{17} \\ \dfrac{1}{\sigma_{cd}}\dfrac{\bar{\rho}}{\tilde{\omega}}\dfrac{\partial \tilde{k}}{\partial x_j}\dfrac{\partial \tilde{\omega}}{\partial x_j}; & \text{Menter–BSL}^{12} \end{cases}$$

$$P_\omega = C_{\omega_p}\bar{\rho}C_{\mu_1}\left(\frac{\partial \tilde{u}_i}{\partial x_j} + \frac{\partial \tilde{u}_j}{\partial x_i}\right)\frac{\partial \tilde{u}_i}{\partial x_j} \tag{26}$$

Note that P_ω is often written as $C_{\omega_p}(\tilde{\omega}/\tilde{k})P_k$. This only applies when the production term for $\tilde{k}$ is evaluated based on the RANS expression for μ_t.

Settles et al. Configuration

The first application of the hybrid RANS/LES turbulence model was the geometry and conditions taken from Refs. 45 and 47. This geometry consists of a supersonic attached flow that separates from a backward facing step and reattaches on an inclined surface farther downstream. The inclined aft surface angle (20-deg) closely mimics the class of cavities typically employed for flameholding purposes. The flowfield geometry and near-field grid system are shown in Fig. 18. The grid upstream of the step had dimensions of $37 \times 33 \times 69$. The grid dimensions downstream of the step were $237 \times 33 \times 109$. The computational domain extended 8.75 step heights downstream of the step. Clustering was performed near all walls and in the anticipated region of shear layer reattachment along the aft surface. The grid points were equally distributed in the spanwise direction, which extended 1.5 step heights. A span of 3 step heights was also considered to confirm that the default width of 1.5 step heights was sufficient. A high degree of grid isotropy (aspect ratios were of order one) was maintained throughout the cavity region (anticipated LES domain) to resolve properly the large eddy structures. This grid was generated based on results from a grid-resolution study for this configuration as described in Ref. 18. The inflow conditions were obtained from a separate calculation

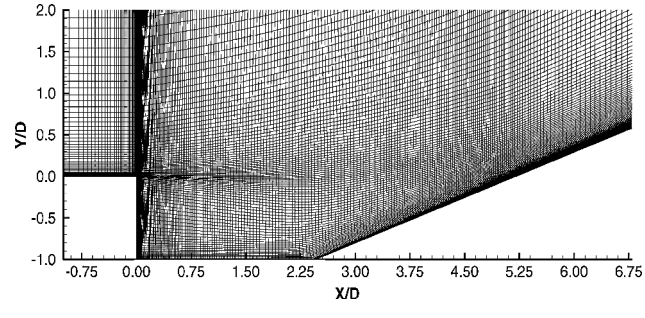

Fig. 18 Cavity near-field grid for the Settles et al. configuration.

that allowed the freestream flow to develop along a flat plate until the momentum thickness one step height upstream of the cavity matched the properties measured in the experiment. A RANS calculation (with the Menter[12] k–ω turbulence model) was used to obtain this inflow profile. The nominal inflow Mach number, pressure, and temperature were 2.92, 21.2 kPa, and 95.37 K, respectively. The far-field boundary was placed at a sufficient distance to allow the enforcement of slip conditions without wave reflections corrupting the region of interest. Homogeneous turbulence was assumed in the spanwise z direction; hence, periodic boundary conditions were enforced at these boundaries. All walls were treated as no-slip adiabatic surfaces, and extrapolation was employed at the outflow plane.

The calculations were performed with the Roe flux difference split scheme with the MUSCL parameter κ chosen as $\frac{1}{3}$. Simulations were carried out with the smooth flux limiter of Krist et al.[24] and a fully second-order accurate Van Leer ENO limiter (see Ref. 23). Both limiters performed well in the channel flow simulations discussed earlier. A comparison of results obtained for this configuration with each limiter showed that a larger fraction of the turbulence was resolved when the ENO limiter was employed. Hence, this limiter was retained for all results discussed later. The dual time-stepping strategy was used for the temporal integration, which combined a DAF method for integration in pseudotime, with a three-point backwards finite difference approximation for integration in real time. Values chosen for the physical time step, subiteration Courant–Friedrichs–Lewy constraint, subiteration convergence criteria (normalized), and maximum number of subiteration steps were 0.1 μs, 3.5, 0.01, and 5, respectively.

All hybrid RANS/LES solutions were initialized based on solutions obtained from two-dimensional RANS simulations. The flowfield was then allowed to evolve (in a time-accurate manner) for a minimum of 10 characteristic time intervals to establish a statistically stationary state. The characteristic timescale was defined in this effort as the time required for a freestream particle to traverse from the separation point (rearward-facing step) to the point of reattachment along the inclined surface (roughly 0.2 ms). On establishment of a statistically stationary state, the data were ensemble averaged by spatially averaging in the homogeneous direction and temporally averaging over a time span that exceeded 10 characteristic flow-through times. The sampling interval was 0.5 μs.

Several calculations were performed to determine appropriate constants for the SGS turbulence equations. At equilibrium (defined when production balances dissipation), the effective Smagorinsky constant implied by the Yoshizawa and Horiuti[46] model is given by the expression

$$(C_s)^2 = \sqrt{2} C_{\mu_2} \left(C_{\mu_2} / C_{d_2} \right)^{\frac{1}{2}} \tag{27}$$

The value of C_s implied by the Yoshizawa and Horiuti model is 0.126 when the default values of 0.05 and 1.0 are used for C_{μ_2} and C_{d_2}, respectively. There is no universal value for this Smagorinsky constant, but the LES community has typically endorsed values on the order of 0.2 for homogeneous turbulence and 0.065 for shear flows.[48] Initial calculations used a reduced value of 0.02075 for C_{μ_2} to recover the accepted Smagorinsky constant for shear flows. This value, however, proved too dissipative with the present second-order upwind numerical framework. The numerical dissipation of these schemes is on the same order as the SGS viscosity, Δ^2; hence, one might expect lower values to be required. A value of $C_{\mu_2} = 0.008232$ was found to unlock adequate levels of resolved turbulence energy in the simulations. This value enforces a Smagorinsky constant of 0.0325 (half the standard value for shear flows) under equilibrium conditions. A similar calibration was performed to determine an acceptable value for C_{DES} in the two-equation variant of the DES model for comparison with the present approach. This model does not reduce to a recognizable Smagorinsky expression at equilibrium, and so the value was changed arbitrarily from the calibrated value[4] of 0.61 (based on calculations of homogeneous turbulence). This constant had to be reduced to 0.1 to yield adequate levels of resolved turbulence for this configuration, given the present numerical framework.

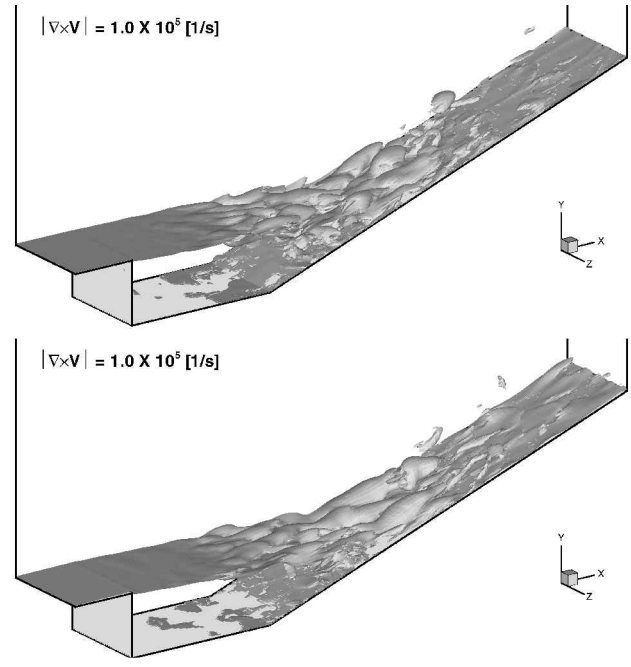

Fig. 19 Snapshot of a vorticity isosurface for the Settles et al. configuration: top, blended RANS/LES and bottom, DES.

Instantaneous images of a vorticity isosurface (1×10^5 1/s) extracted from the hybrid RANS/LES and DES methods are shown in Fig. 19. The results from both models are qualitatively similar. After separation from the step, elongated two-dimensional Kelvin–Helmholtz structures develop and eventually break down into three-dimensional turbulent structures just upstream of reattachment. The inclined aft surface does not allow acoustic disturbances to reflect directly back toward the rearward facing step, weakening the feedback mechanism as compared with rectangular cavities. Without this feedback mechanism, the transition from a steady RANS boundary layer to a free shear flow with active turbulent structures is delayed. This problem is common to all hybrid RANS/LES approaches and can be remedied by supplying the upstream boundary layer with turbulent structures, as discussed in Refs. 10 and 49.

Time-averaged properties extracted from the hybrid RANS/LES and DES data sets are compared with measurements in Fig. 20. Also included in Fig. 20 is a pure Menter–BSL[12] RANS calculation with allowances for a compressibility correction. The convective Mach number for the free shear layer in this flow is approximately 1.5, which indicates that the effects of compressibility are important. The compressibility correction chosen was that of Wilcox.[16] This correction was not applied to the hybrid calculations because the free shear region is governed by the SGS model rather than the RANS model. A comparison of the shear layer velocity profiles shows that all three models overpredict the degree of expansion into the cavity. The shear layer spreading rate predicted by the compressibility corrected RANS model compares well with measurements. (The disagreement shown in Fig. 20 is primarily a result of the bulk expansion into the cavity, rather than the spreading rate.) The initial shear spreading rate is underpredicted by both hybrid models due to the delay of resolved TKE production that was discussed earlier. The agreement in spreading rate is considerably more favorable farther downstream, once the turbulent structures have time to develop. The pressure along the ramped surface and profiles of velocity and pressure normal to this surface are also shown in Fig. 20. In these images, x^* is the wetted distance along the ramp, y^* the perpendicular distance from the surface, and u^* the velocity component parallel to the surface. The surface pressure trace is predicted well by both hybrid approaches, as are the recovery rates of the velocity profiles downstream

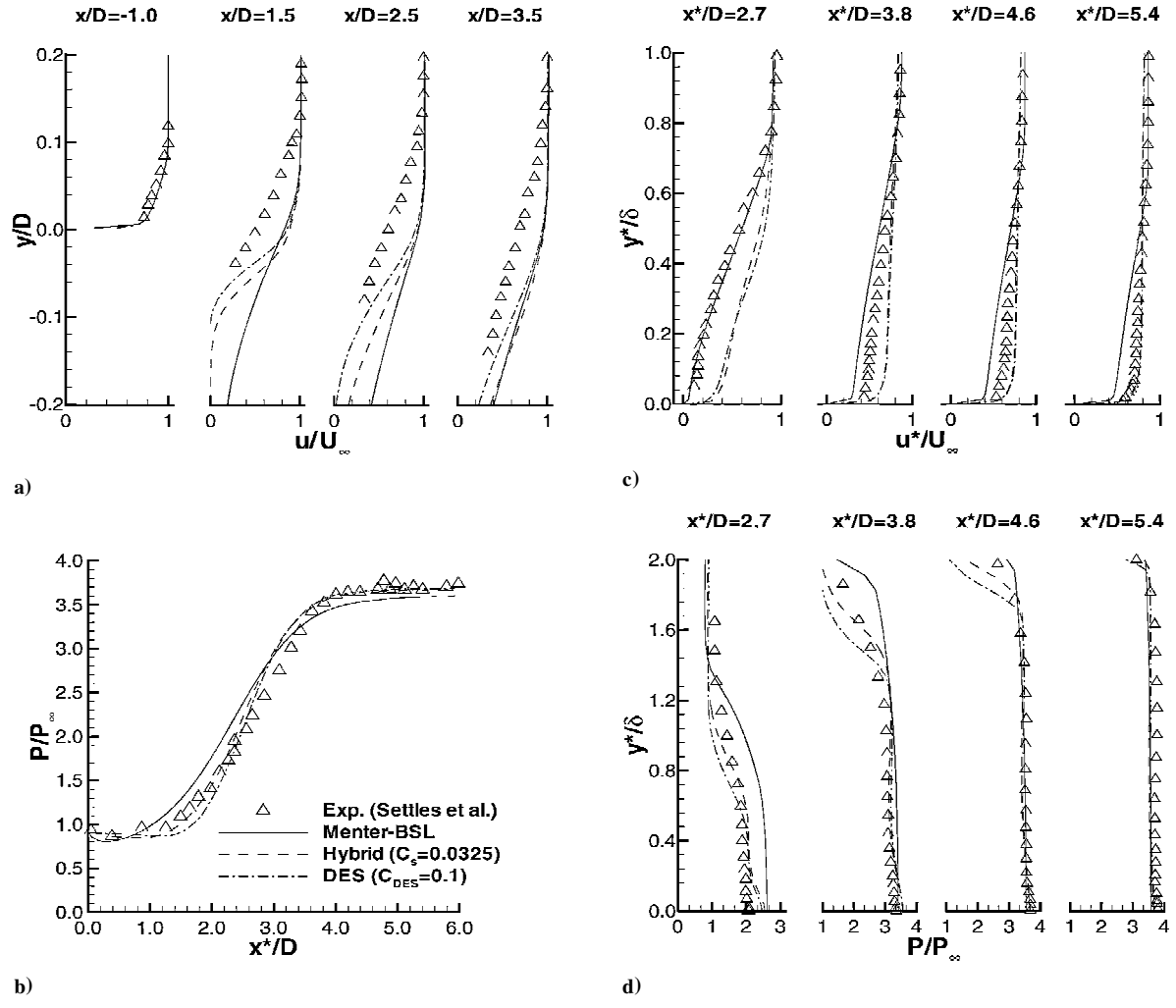

Fig. 20 Settles et al. configuration: a) shear velocity profiles, b) cavity surface pressure, c) velocity profiles in boundary-layer recovery region, and d) pressure profiles in boundary-layer recovery region.

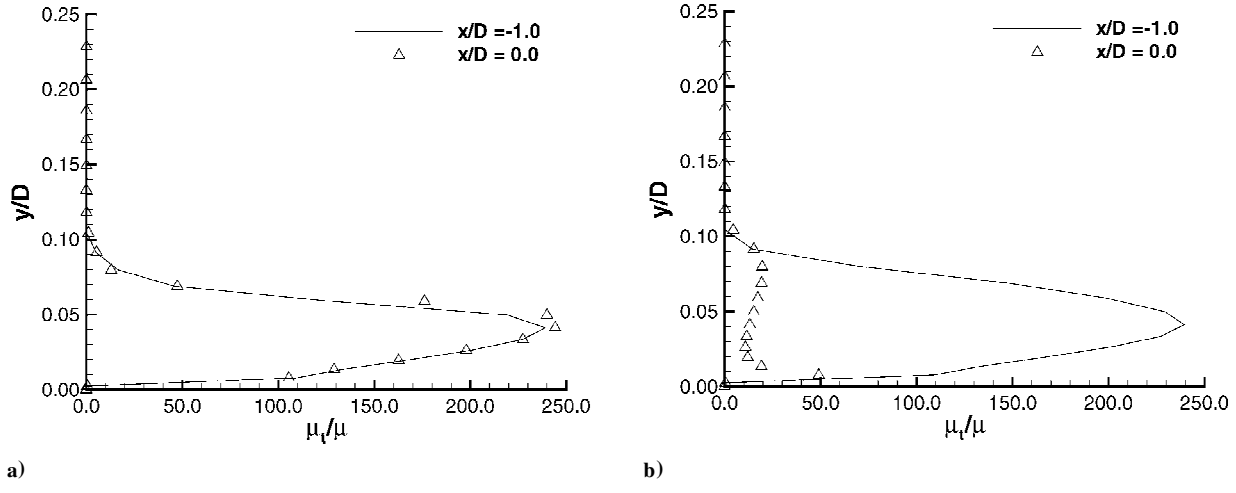

Fig. 21 Ratio of turbulent to laminar viscosity in the approach boundary layer of the Settles et al. configuration: a) blended RANS/LES and b) DES.

of shear layer reattachment (last three stations). The good agreement between the RANS profile and measurements at the first station (reattachment point) is somewhat fortuitous, given the overexpansion of the shear layer into the cavity predicted by the model. The delay in the velocity recovery at stations farther downstream, however, is a deficiency common to all RANS models known to the authors. The hybrid models appear to handle this recovery process quite well.

Although the data comparisons between the DES and hybrid RANS/LES models show many similarities, one important difference should be noted. A plot of the turbulent to laminar viscosity ratio in the upstream boundary layer (Fig. 21) shows a sharp decline in the eddy viscosity upstream of the separation point when the DES model is employed. The hybrid RANS/LES model, on the other hand, maintained the RANS level of turbulent viscosity. The DES model can be recast into a framework that is consistent with

the blending approach proposed in this effort. This is accomplished by rewriting the dissipation term of the DES turbulence kinetic energy equation as

$$\text{DES TKE dissipation} = (F_{\text{DES}})\left(\bar{\rho}\tilde{k}^{\frac{3}{2}}/\ell_{\text{RANS}}\right) + (1 - F_{\text{DES}})C_{\text{DES}}\left(\bar{\rho}\tilde{k}^{\frac{3}{2}}/\Delta\right) \tag{28}$$

where the blending function F_{DES} is given by

$$F_{\text{DES}} = \text{AINT}[\text{minimum}(C_{\text{DES}}\Delta/\ell_{\text{RANS}}, 1.0)] \tag{29}$$

A comparison of instantaneous images of the hybrid RANS/LES blending function and the effective DES blending function is given in Fig. 22. Figure 22 highlights the danger in choosing a value of C_{DES} that is too small and/or using a grid with nearly isotropic cells in wall-bounded regions. As indicated by Fig. 22, nearly the entire attached boundary layer is tagged as an LES region. Clearly this is not the desired behavior and is the cause of the rapid decline in eddy viscosity seen in Fig. 21. The hybrid RANS/LES approach developed in this effort takes into account the turbulent flow structure, as well as the grid spacing, to determine the switching from RANS to LES. This provides more control over the blending process and removes much of the burden from the grid generation process. As a final note, the hybrid RANS/LES calculation was repeated using the Wilcox[17] model as the parent RANS model. Results obtained were practically identical to the results discussed earlier. This trend was expected because the RANS model is only invoked in attached wall-bounded portions of the flow, a region that both models are well calibrated for.

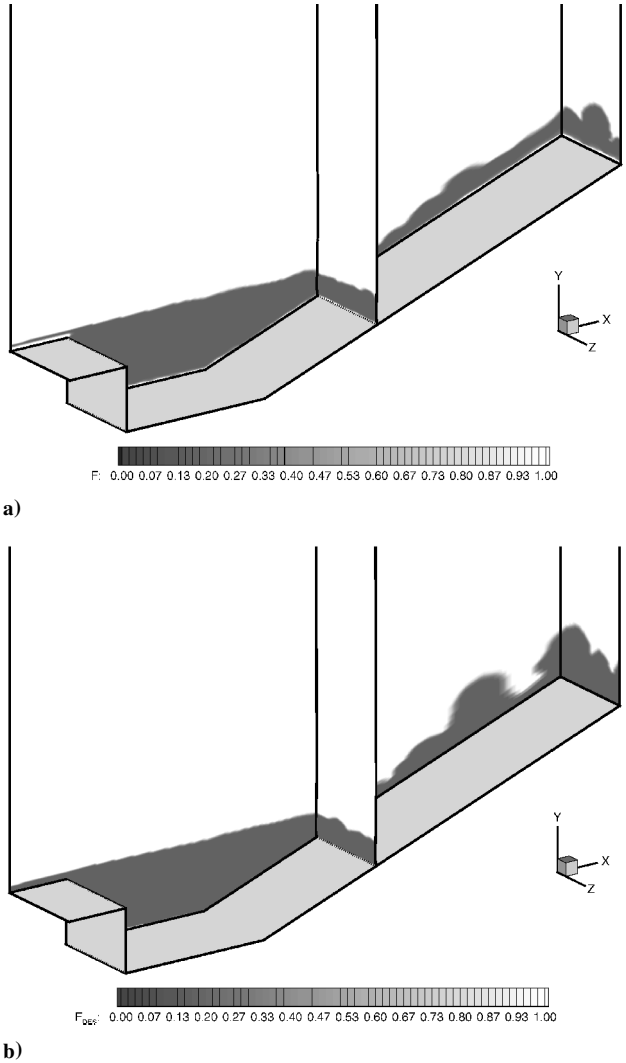

Fig. 22 Snapshot of the blending functions for the Settles et al. configuration: a) blended RANS/LES and b) DES.

AFRL/PRA Cavity

The second case considered was a Mach 2.0 flow over a rectangular cavity with a length to depth ratio of 7.76. The cavity is embedded into a divergent (2.2-deg) surface, as is often the case when these devices are used as flame holders in scramjet combustors. The total grid system considered for this generic flame holder is shown in Fig. 23. The grid generated for the main duct had dimensions of $321 \times 53 \times 81$. The grid dimensions within the cavity were $201 \times 53 \times 41$. Homogeneous turbulence was assumed in the spanwise y direction; hence, periodic boundary conditions were enforced at these boundaries. (The grid points were equally distributed over a span of three cavity depths.) The inflow conditions were obtained from a separate calculation of the flow through the Mach 2.0 facility nozzle, which operated nominally at stagnation conditions of 344.74 kPa and 300 K. The grid was clustered near all solid surfaces. A no-slip adiabatic condition was imposed at all walls, and a zero-gradient condition was enforced at the outflow boundary. Grid aspect ratios were kept under 10 in the vicinity of the cavity. All numerical algorithm parameters were set equal to those used for the Settles configuration, with the exception of the physical time step, which was reduced by a factor of 2 to 0.05 μs. All hybrid RANS/LES solutions were initialized based on solutions obtained from two-dimensional RANS (Menter–BSL[12]) simulations. The data described were extracted from the simulations after the flow had evolved from this initialization (in a time-accurate manner) for eight characteristic time intervals (defined as the time required for a freestream particle to traverse the cavity).

Qualitative results extracted from the hybrid RANS/LES simulation are shown in Fig. 24. Figure 24 highlights one snapshot of the cavity oscillation cycle through a visualization of a numerical schlieren image (approximated by the density gradient magnitude). From this image, disturbances can be observed both outside and within the cavity. The pressure oscillations within the cavity are to a large extent driven by the impingement of shed vortices at the corner of the aft wall. This occurrence creates an upstream traveling pressure wave within the cavity, providing the feedback mechanism to sustain the oscillation cycle. A detailed description of this self-sustaining oscillation process can be found in Refs. 50 and 51. The deformation of the shear layer caused by these oscillations forms resonating shock waves above the cavity. The shear layer deflection also causes a periodic ingestion and expulsion of flow into and out of the cavity. In a scramjet engine, the ingestion process provides the cavity with oxidizer, whereas the ejection phase provides the main flow with hot combustion products. Multiple trapped vortices

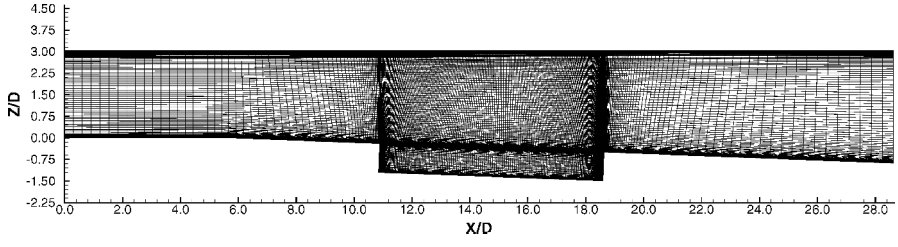

Fig. 23 Grid for the generic cavity flame holder.

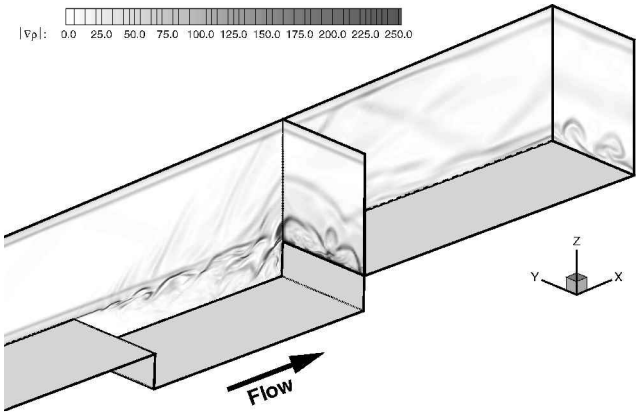

Fig. 24 Snapshot of the density gradient magnitude (numerical schlieren) for the generic cavity flame holder.

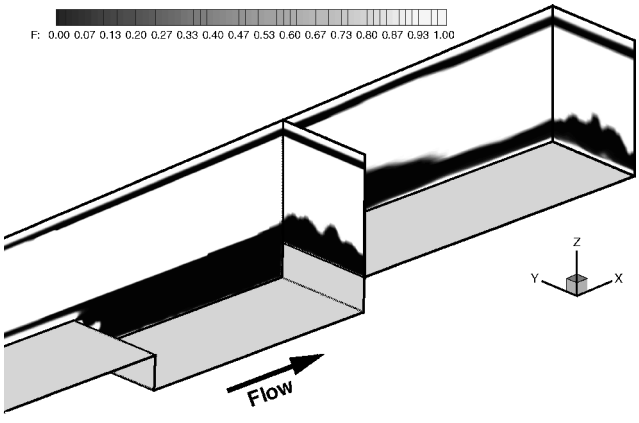

Fig. 25 Snapshot of the blending function for the generic cavity flame holder.

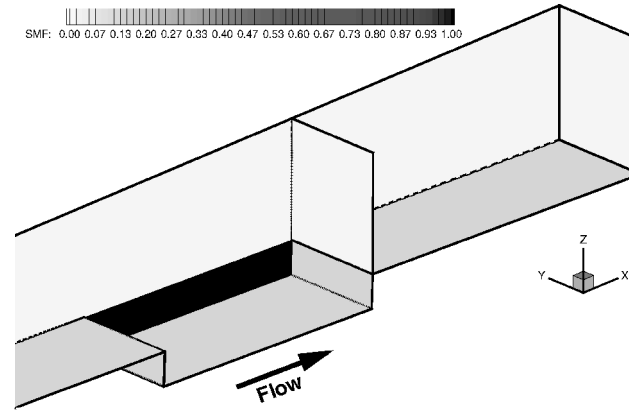

Fig. 26 Snapshot of the cavity fluid mass decay, $t = 0$ ms.

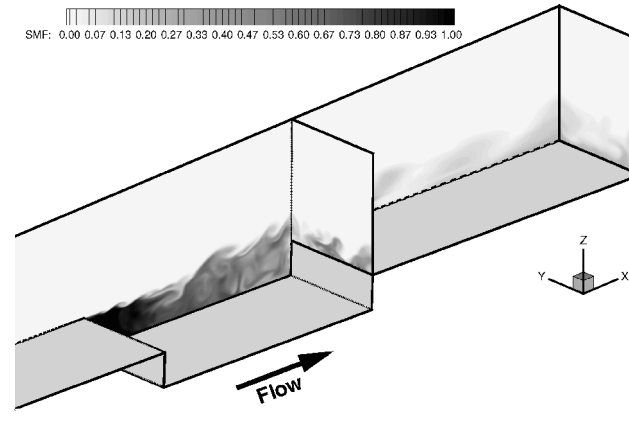

Fig. 27 Snapshot of the cavity fluid mass decay, $t = 1$ ms.

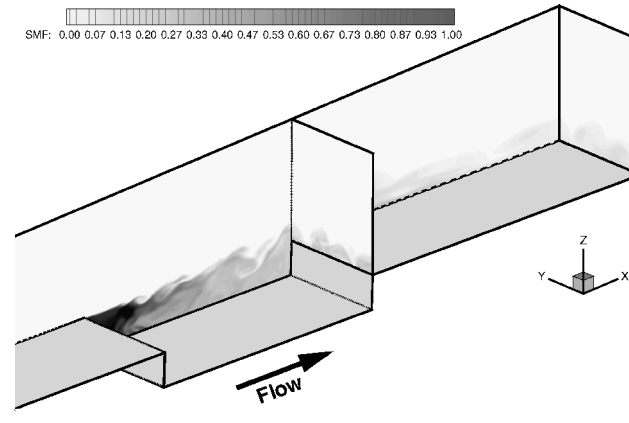

Fig. 28 Snapshot of the cavity fluid mass decay, $t = 2$ ms.

are evident in the cavity, and, at isolated instances in time, this cavity becomes essentially closed due to shear layer deflections that impinge near the lower aft wall corner.

A close examination of the schlieren image shows that the hybrid RANS/LES model is qualitatively behaving as designed. The approach boundary layer and the boundary layer along the opposite (top) wall exhibit quasi-steady RANS properties, whereas the flow in the cavity is obviously quite dynamic, showing that the LES model is active in this region. The RANS and LES regions are more clearly exposed by examining an instantaneous snapshot of the blending function [Eq. (9)]. The freestream region above the cavity showed negligible levels of modeled (RANS and SGS) viscosity. Based on this observation, the image shown in Fig. 25 was forced to resemble a RANS region if the modeled to molecular viscosity ratio was less than 0.1. This operation was performed to better visualize the relevant RANS and LES regions. Figure 25 clearly indicates that the switching function is retaining the RANS model in the approach boundary layer and opposite wall boundary layer. Shock waves emanating from the oscillating shear layer above the cavity interact with the boundary layer along the top wall. However, this interaction is not strong enough to cause separation. Hence, the switching function maintains the RANS model equations throughout this shock/boundary-layer interaction region. The switching function enforced a substantial LES region near the wall downstream of the cavity, where large coherent vortical structures are traversing along the wall.

The mass exchange between the main stream and cavity determines the characteristic cavity residence time, which is of fundamental importance when sizing flame holders. The mass exchange process was analyzed by tagging the fluid within the cavity after a periodic state had been established. The fluid beneath the imaginary line that connects the top of the cavity fore wall to the top of the cavity aft wall was tagged as black air, whereas the fluid above this imaginary line was tagged as white air. The calculation was then reinitiated, and the mass exchange process was monitored as a function of time. Note that the tagging process in no way changes the fluid state, it simply serves as a marker for monitoring how the fluid in the cavity interacts with the main stream flow.

Several snapshots of the time evolution of the mass exchange process are given in Figs. 26–28. The intense cavity oscillation cycle forms multiple trapped vortices within the cavity. Initial packets of main stream air enter the aft end of the cavity as the shear layer impinges on the cavity aft wall. These packets follow the periphery of a trapped vortex that is positioned near the aft wall. These packets mix with adjacent vortices after several oscillation cycles. The main stream fluid continues to migrate in this manner and eventually reaches the trapped vortex adjacent to the cavity fore wall. The local residence time associated with fluid trapped near the fore wall of

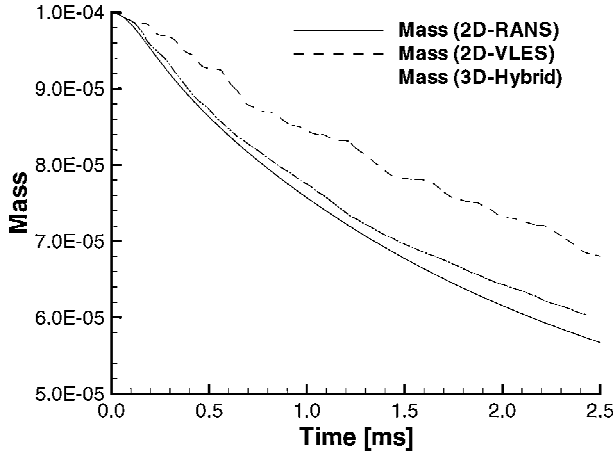

Fig. 29 Time history comparison of cavity fluid mass decay.

the cavity is substantially greater than the residence time associated with the fluid present near the aft wall. Detailed images such as this can provide the designer with crucial information that can guide how the cavity should be fueled for optimal performance.

The mass exchange process can be quantified in a global sense by defining a global characteristic residence time. A global residence time estimate is required in perfectly stirred reactor models used for mapping out flame holding characteristics. The cavity residence time is defined as the timescale associated with the decay rate of the fluid within the cavity, due to mass exchange with the main stream fluid. Typically, it is assumed that the decay of the cavity fluid time history can be fit to an exponential curve, that is,

$$m(t) \approx \exp[-t/\tau] \tag{30}$$

where τ is the residence time. Thus, if the cavity fluid mass decay history is known as a function of time, then the residence time can be deduced. The cavity residence time was extracted from the computational fluid dynamics data by performing a nonlinear (exponential) least-squares fit to the recorded time history of the cavity fluid mass. The tagged cavity air was initialized based on the geometric line of the cavity (rather than the dividing stagnation streamline). Thus, the least-squares fit could not be performed until sufficient time had passed to allow the tagged cavity fluid initially present above the stagnation stream line to convect out of the domain. Unfortunately, the error associated with the least-squares fit was significant, given the relatively small sample of mass decay gathered from the three-dimensional hybrid simulations. Instead, general trends were ascertained by comparing the mass decay time history with two-dimensional data (Fig. 29) taken from Ref. 52. Results with and without the use of a turbulence model were extracted from Ref. 52. The resolved large-scale structures are the primary mechanisms controlling the decay of cavity air in the hybrid RANS/LES and two-dimensional (laminar) simulations. The mass decay given by the steady RANS simulation, however, is driven exclusively by the modeled turbulent diffusion processes (controlled by the eddy viscosity and turbulent Schmidt number). The hybrid RANS/LES mass decay history is bounded by the two-dimensional mass decay time histories. The decay rate predicted by the hybrid RANS/LES simulation is considerably faster than that given by the two-dimensional laminar simulation. Both simulations exhibited large-scale structures of similar magnitude; however, the interface between the cavity and duct air is planar in the two-dimensional simulation. Therefore, even if the amplitude of the shear layer oscillation is similar to that given by the three-dimensional-hybrid solutions, one would expect a more rapid decay rate in the three-dimensional case due to the larger interface area. Note that the hybrid RANS/LES decay rate is very close to that predicted by the steady-state RANS simulation. This suggests that the assumed value of the turbulent Schmidt number (0.5 in the present simulations) was a reasonable estimate when used in conjunction with the Menter–BSL turbulence model.[12] This result is fortuitous because the mass exchange process varies significantly with a change in cavity shape, a result that can not be predicted by steady-state simulations. The residence times extracted from the two-dimensional simulations with and without the turbulence model were 1.8 and 2.9 ms, respectively. The residence time extracted from the hybrid RANS/LES simulation would appear to be on the order of 2.0 ms.

Conclusions

A hybrid RANS/LES model has been developed that blends the RANS and SGS model equations using a function that depends on local turbulent flow properties and mesh spacing. The blending function was designed to retain the RANS equation set in attached wall-bounded flow regions regardless of mesh spacing. This feature avoids a relaminarization of the flow that can occur with other hybrid models in wall-bounded regions where the mesh is refined in all directions. Free shear regions are treated as LES regions, provided that the SGS viscosity is less than the RANS viscosity. Standard second-order accurate algorithms have been thoroughly tested for a pure LES of fully developed channel flow and supersonic flow past a blunt base. The results of this effort suggests that a second-order accurate upwind-biased numerical framework can be retrofitted for hybrid RANS/LES calculations. A simple means of controlling numerical dissipation within a second-order accurate framework was shown to resolve turbulence structures at scales similar to those obtained using higher-order methods (using similar grids) for the fully developed channel flow problem. Common TVD flux limiters were found to be overly dissipative, even at substantially reduced numerical dissipation levels. The ENO limiters or the smooth limiters discussed in this work proved to be more viable options. Data extracted from simulations of supersonic flow past a blunt annular sting using a MILES technique compared well with measurements. Of particular interest was the accurate prediction of uniform pressure along the sting base, a result rarely seen when RANS models are employed. Random forcing based on a prescribed PDF that matched all relevant first- and second-order single-point correlations was found to have a negligible impact on the far-field turbulence statistics. This result is consistent with the existing literature. Better options exist for prescribing turbulent inflow conditions that account for the coherency of the incoming fluctuations; unfortunately, these methods require more information than a RANS profile can provide.

The hybrid RANS/LES formulation was applied to two separate recessed cavity flowfields. The results for the Settles et al. configuration were compared with those obtained using a two-equation DES formulation and with measurements. Both the hybrid RANS/LES and DES models showed a delayed transition from a fully unresolved (modeled) RANS attached boundary layer to a mostly resolved LES free shear layer. This behavior is primarily caused by the absence of any resolved levels of turbulence in the approach boundary layer. This situation is improved greatly if a mechanism exists to encourage instabilities as seen in the rectangular cavity simulations. Both hybrid models showed improvements over the RANS model in the prediction of velocity profiles downstream of separation. The slow recovery rate from a free shear profile to an attached boundary-layer profile is a common deficiency of RANS models. The second cavity configuration considered involved a generic flame holder concept for a scramjet engine. An analysis of the mass exchange process for this rectangular cavity flow showed that the residence time of fluid particles initially present near the front of the cavity was substantially larger than that of particles near the aft end of the cavity. This type of detailed data, which can be quite useful when choosing fueling schemes for the cavity, cannot be accurately extracted from steady-state RANS calculations.

Acknowledgments

This study was supported by and performed at Wright–Patterson Air Force Base, under a Phase 2 Small Business Innovation Research Contract (Contract F33615-00-C-2017, Technical Monitor Douglas Davis). Additional support included a grant of computer time from the ASC Department of Defense High Performance Computing center. A special thanks is given to N. Okong'o for providing the channel flow direct numerical simulation, large eddy simulation,

and measured data. T. Mathur is acknowledged for providing data files of measurements taken from the University of Illinois base flow experiments, as well as filling in details concerning the experimental setup. A sincere thanks is also extended to J. White of the NASA Langley Research Center for many helpful discussions involving modifications to the VULCAN flow solver.

References

[1]Gruber, M. R., Baurle, R. A., Mathur, T., and Hsu, K.-Y., "Fundamental Studies of Cavity-Based Flameholder Concepts for Supersonic Combustors," *Journal of Propulsion and Power*, Vol. 17, No. 1, 2001, pp. 146–153.

[2]Sinha, N., Dash, S. M., and Chidambaram, N., "A Perspective on the Simulation of Cavity Aeroacoustics," AIAA Paper 98-0286, Jan. 1998.

[3]Baurle, R. A., and Gruber, M. R., "A Study of Recessed Cavity Flowfields for Supersonic Combustion Applications," AIAA Paper 98-0938, Jan. 1998.

[4]Strelets, M., "Detached Eddy Simulation of Massively Separated Flows," AIAA Paper 2001-0879, Jan. 2001.

[5]Spalart, P. R., Jou, W.-H., Strelets, M., and Allmaras, S. R., "Comments on the Feasibility of LES for Wings, and on a Hybrid RANS/LES Approach," 1st Air Force Office of Scientific Research International Conf. on DNS/LES, Aug. 1997.

[6]Speziale, C. G., "Turbulence Modeling for Time Dependent RANS and VLES: A Review," *AIAA Journal*, Vol. 36, No. 2, 1998, pp. 173–184.

[7]Arunajatesan, S., and Sinha, N., "Towards Hybrid LES-RANS Computations of Cavity Flowfields," AIAA Paper 2000-0401, Jan. 2000.

[8]Batten, P., Goldberg, U., and Chakravarthy, S., "Sub-Grid Turbulence Modeling for Unsteady Flow with Acoustic Resonance," AIAA Paper 2000-0473, Jan. 2000.

[9]Zhang, H.-L., Bachman, C. R., and Fasel, H. F., "Application of a New Methodology for Simulations of Complex Turbulent Flows," AIAA Paper 2000-2535, June 2000.

[10]Batten, P., Goldberg, U., and Chakravarthy, S., "LNS—An Approach Towards Embedded LES," AIAA Paper 2002-0427, Jan. 2002.

[11]Spalart, P. R., and Allmaras, S. R., "A One-Equation Turbulence Model for Aerodynamic Flows," AIAA Paper 92-0439, Jan. 1992.

[12]Menter, F. R., "Zonal Two Equation k–ω Models for Aerodynamic Flows," AIAA Paper 93-2906, July 1993.

[13]Shur, M., Spalart, P. R., Strelets, M., and Travin, A., "Detached-Eddy Simulaion of an Airfoil at High Angle of Attack," *Engineering Turbulence Modelling and Experiments–4*, edited by W. Rodi and D. Laurence, Elsevier, 1999.

[14]Constantinescu, G. S., and Squires, K. D., "LES and DES Investigations of Turbulent Flow Over a Sphere," AIAA Paper 2000-0540, Jan. 2000.

[15]Forsythe, J. R., and Hoffmann, K. A., "Detached-Eddy Simulation of a Supersonic Axisymmetric Base Flow with an Unstructured Solver," AIAA Paper 2000-2410, June 2000.

[16]Wilcox, D. C., *Turbulence Modeling for CFD*, 1st ed., DCW Industries, Inc., 1993.

[17]Wilcox, D. C., *Turbulence Modeling for CFD*, 2nd ed., DCW Industries, Inc., 1998.

[18]Fan, T. C., Tian, M., Edwards, J. R., Hassan, H. A., and Baurle, R. A., "Validation of a Hybrid Reynolds-Averaged/Large-Eddy Simulation Method for Simulating Cavity Flameholder Configurations," AIAA Paper 2001-2929, June 2001.

[19]Fan, T. C., Xiao, X., Edwards, J. R., Hassan, H. A., and Baurle, R. A., "Hybrid RANS/LES Simulation of a Shock Wave/Boundary Layer Interaction," AIAA Paper 2002-0431, Jan. 2002.

[20]Nikitin, N. V., Nicoud, F., Wasistho, B., Squires, K. D., and Spalart, P. R., "An Approach to Wall Modeling in Large-Eddy Simulations," *Physics of Fluids*, Vol. 12, July 2000, pp. 1629–1632.

[21]White, J. A., and Morisson, J. H., "Pseudo-Temporal Multi-Grid Relaxation Scheme for Solving the Parabolized Navier–Stokes Equations," AIAA Paper 99-3360, June 1999.

[22]VULCAN. http://vulcan-cfd.larc.nasa.gov/ [cited March 2003].

[23]Suresh, A., and Huynh, H. T., "Numerical Experiments on a New Class of Nonoscillatory Schemes," AIAA Paper 92-0421, Jan. 1992.

[24]Krist, S. L., Thomas, J. L., Sellers, W. L., and Kjelgaard, S. O., "An Embedded Grid Formulation Applied to a Delta Wing," AIAA Paper 90-0429, Jan. 1990.

[25]Venkatakrishnan, V., "On the Accuracy of Limiters and Convergence to Steady State Solutions," AIAA Paper 93-0880, Jan. 1993.

[26]Bui, T. T., "A Parallel, Finite-Volume Algorithm for Large-Eddy Simulation of Turbulent Flows," AIAA Paper 99-0789, Jan. 1999.

[27]Swanson, R. C., and Turkel, E., "On Central-Difference and Upwind Schemes," *Journal of Computational Physics*, Vol. 101, No. 2, 1992, pp. 292–306.

[28]Ducros, F., Ferrand, V., Nicoud, F., Weber, C., Darracq, D., Gacherieu, C., and Poinsot, T., "Large-Eddy Simulation of the Shock/Turbulence Interaction," *Journal of Computational Physics*, Vol. 152, No. 2, 1999, pp. 517–549.

[29]Bird, G. A., *Molecular Gas Dynamics and the Direct Simulation of Gas Flows*, Oxford Univ. Press, Oxford, 1994, Appendix 3, pp. 207–210.

[30]Kaltenbach, H.-J., Fatica, M., Mittal, R., Lund, T. S., and Moin, P., "Study of Flow in a Planar Asymmetric Diffuser Using Large-Eddy Simulation," *Journal of Fluid Mechanics*, Vol. 390, July 1999, pp. 151–185.

[31]Lee, S., Lele, S. K., and Moin, P., "Simulation of Spatially Evolving Turbulence and the Applicability of Taylor's Hypothesis in Compressible Flow," *Physics of Fluids*, Vol. 4, No. 7, 1992, pp. 1521–1530.

[32]Urbin, G., Knight, D., and Zheltovodov, A. A., "Large Eddy Simulation of a Supersonic Boundary Layer Using Unstructured Grids," *AIAA Journal*, Vol. 39, No. 7, 2001, pp. 1288–1295.

[33]Eckelmann, H., "The Structure of the Viscous Sublayer and the Adjacent Wall Region in a Turbulent Channel Flow," *Journal of Fluid Mechanics*, Vol. 65, 1974, pp. 439–459.

[34]Kim, J., Moin, P., and Moser, R., "Turbulence Statistics in Fully Developed Channel Flow at Low Reynolds Number," *Journal of Fluid Mechanics*, Vol. 177, 1987, pp. 133–166.

[35]Okong'o, N., and Knight, D., "Compressible Large Eddy Simulation Using Unstructured Grids: Channel and Boundary Layer Flows," AIAA Paper 98-3315, July 1998.

[36]Menon, S., and Chakravarthy, V. K., "Large Eddy Simulations of Premixed Flames in Couette Flow," AIAA Paper 96-3077, July 1996.

[37]Askelvoll, K., and Moin, P., "Large Eddy Simulation of Turbulent Confined Coannular Jets," *Journal of Fluid Mechanics*, Vol. 315, May 1996, PP. 387–412.

[38]Herrin, J. L., and Dutton, J. C., "Supersonic Base Flow Experiments in the Near Wake of a Cylindrical Afterbody," *AIAA Journal*, Vol. 32, No. 1, 1994, PP. 77–83.

[39]Fureby, C., Nilsson, Y., and Andersson, K., "Large Eddy Simulation of Supersonic Base Flow," AIAA Paper 99-0426, Jan. 1999.

[40]Tucker, P. K., and Shyy, W., "A Numerical Analysis of Supersonic Flow over an Axisymmetric Afterbody," AIAA Paper 93-2347, July 1993.

[41]Sahu, J., "Numerical Computations of Supersonic Base Flow with Special Emphasis on Turbulence Modeling," *AIAA Journal*, Vol. 32, No. 7, 1994, pp. 1547–1549.

[42]Chuang, C. C., and Chieng, C. C., "Supersonic Base-Flow Computation Using Higher-Order Turbulence Models," *Journal of Spacecraft and Rockets*, Vol. 33, No. 3, 1996, pp. 374–380.

[43]Suzen, Y. B., Hoffman, K. A., and Foresythe, J. R., "Application of Several Turbulence Models for High Speed Shear Layer Flows," AIAA Paper 99-0933, Jan. 1999.

[44]Rai, M. M., "Navier–Stokes Simulations of Blade Vortex Interaction Using High-Order Accurate Upwind Schemes," AIAA Paper 87-0543, Jan. 1987.

[45]Settles, G. S., Williams, D. R., Baca, B. K., and Bogdonoff, S. M., "Reattachment of a Compressible Turbulent Free Shear Layer," *AIAA Journal*, Vol. 20, No. 1, 1982, pp. 60–68.

[46]Yoshizawa, A., and Horiuti, K., "A Statistically-Derived Subgrid Scale Kinetic Energy Model for Large-Eddy Simulation of Turbulent Flows," *Journal of the Physical Society of Japan*, Vol. 54, 1985, p. 2834.

[47]Horstman, C. C., Settles, G. S., Williams, D. R., and Bogdonoff, S. M., "A Reattaching Free Shear Layer in Compressible Turbulent Flow," *AIAA Journal*, Vol. 20, No. 1, 1981, pp. 79–85.

[48]Ferziger, J. H., "Large Eddy Simulation," ICASE/NASA Langley Research Center Short Course on Turbulent Flow Modeling and Prediction, March 1994.

[49]Kannepalli, C., Arunajatesan, S., and Dash, S. M., "RANS/LES Methodology for Supersonic Transverse Jet Interactions with Approach Flow," AIAA Paper 2002-1139, Jan. 2002.

[50]Heller, H. H., and Bliss, D. B., "The Physical Mechanism of Flow-Induced Pressure Fluctuations in Cavities and Concepts for Their Supression," AIAA Paper 75-491, Jan. 1975.

[51]Rockwell, D., and Naudascher, E., "Review—Self-Sustaining Oscillations of Flow Past Cavities," *Journal of Fluids Engineering*, Vol. 100, No. 6, 1978, pp. 152–165.

[52]Baurle, R. A., Tam, C.-J., and Dasgupta, S., "Analysis of Unsteady Cavity Flows for Scramjet Applications," AIAA Paper 2000-3617, July 2000.

P. Givi
Associate Editor